ADVANCING EARTH AND SPACE SCIENCES

JGR Earth Surface

RESEARCH ARTICLE

10.1029/2023JF007266

Key Points:

- In a semi-arid landscape, transitions to drier climates cause increases in erosion lasting on the order of 10^3–10^4 years
- Wildfire activity and pine tree abundance correlate with enhanced erosion
- Anthropogenic drying trends and increased wildfire in southwestern North America will promote enhanced erosion rates

Supporting Information:

Supporting Information may be found in the online version of this article.

Correspondence to:

S. E. Staley,
spencer.staley@dri.edu

Citation:

Staley, S. E., Fawcett, P. J., Jiménez-Moreno, G., Anderson, R. S., Markgraf, V., & Brown, E. T. (2023). Long-term landscape evolution in response to climate change, ecosystem dynamics, and fire in a basaltic catchment on the Colorado Plateau. *Journal of Geophysical Research: Earth Surface*, *128*, e2023JF007266. https://doi.org/10.1029/2023JF007266

Received 17 MAY 2023
Accepted 9 NOV 2023

Author Contributions:

Conceptualization: Spencer E. Staley, Peter J. Fawcett, R. Scott Anderson
Data curation: Spencer E. Staley
Formal analysis: Spencer E. Staley
Funding acquisition: Peter J. Fawcett
Investigation: Spencer E. Staley, Gonzalo Jiménez-Moreno, R. Scott Anderson, Vera Markgraf, Erik T. Brown
Methodology: Spencer E. Staley
Visualization: Spencer E. Staley
Writing – original draft: Spencer E. Staley

Long-Term Landscape Evolution in Response to Climate Change, Ecosystem Dynamics, and Fire in a Basaltic Catchment on the Colorado Plateau

Spencer E. Staley[1,2], Peter J. Fawcett[1], Gonzalo Jiménez-Moreno[3], R. Scott Anderson[4], Vera Markgraf[4], and Erik T. Brown[5]

[1]University of New Mexico, Albuquerque, NM, USA, [2]Desert Research Institute, Reno, NV, USA, [3]Universidad de Granada, Granada, Spain, [4]Northern Arizona University, Flagstaff, AZ, USA, [5]University of Minnesota, Duluth, Duluth, MN, USA

Abstract Predicting responses of semi-arid to montane landscapes in southwestern North America to ongoing anthropogenic changes requires understanding of past interplay among geomorphic, ecologic, and climatic factors. This study utilizes modern weathering and sediment transport processes to inform the interpretation of a 250-kyr lacustrine sediment record of paleoecology, hydrology, and erosion from a small, closed basin, basaltic catchment on the southwestern edge of the Colorado Plateau. Geochemical and mineralogical analyses of bedrock, colluvium, and lake sediments indicate that clastic sediments in the basin are a mixture of local physical weathering products (albite and ilmenite) and eolian dust (quartz, illite, and zircon). Dust fractions increase during glacial periods coincident with lower overall sedimentation rates, suggesting this pattern results from decreased local erosion rates and not increased dust deposition. Titanium counts from X-ray fluorescence core scanning, a proxy for ilmenite content, traces past local erosion rates. The highest erosion rates, inferred from the highest Ti counts, follow climatic transitions toward interglacial conditions (Marine Isotope Stage 5e, 3a, and the Holocene), periods characterized by vegetation changeover (observed in the core's palynology), higher temperatures (piñon-juniper-oak pollen abundance), lower effective precipitation (shallow lake facies), and increased wildfire activity (microscopic charcoal particle counts and sizes). While brief inferred episodes of erosion occur following abrupt transitions to cooler and wetter conditions, indicated by the abundance of subalpine tree (spruce and fir) pollen and deeper lake facies, landscapes appear more stable during glacial periods. This long-term perspective suggests that aridification and resulting vegetation succession and increased wildfires will increase erosion rates in similar settings regionwide.

Plain Language Summary Many humans depend on the dry landscapes of southwestern North America for their livelihood. Identifying potential challenges associated with human-caused climate change in the decades and centuries to come requires us to examine how these landscapes have responded to past changes in vegetation, precipitation, and forest fires. This study focuses on a lake sediment core from a small watershed on the southwestern edge of the Colorado Plateau as an archive of the past 250 thousand years, a period spanning multiple significant climate changes. Taken together, indicators of local erosion, climate, fire activity, and plant communities found in lake sediments demonstrate this landscape is shaped by climate change. While transitions toward wetter and cooler conditions can stimulate erosion briefly, the longest lasting increases in erosion occur following transitions toward warmer and drier conditions with greater forest fire activity. Because these types of environmental changes are occurring today due to human-caused climate change, we expect erosion rates to remain high or increase in similar settings across the region.

1. Introduction

Understanding how a landscape undergoes geomorphic change in response to abrupt environmental perturbation is vital to predicting effects of anthropogenic climate change and requires knowledge of the local climatologic, geologic, and ecologic factors affecting weathering and erosion. While generating these holistic perspectives is straightforward using modern instrumentation, landscape responses are often complex with lag times exceeding our observational range. For example, measurable geomorphic effects such as decreased slope stability and higher catchment sediment yields that are expected to result from anthropogenically enhanced droughts, extreme precipitation events, overgrazing, more intense and widespread wildfires, and forest ecosystem changeover have yet to be detected by observations spanning the last ~50 years in many locations across western North America

Writing – review & editing: Spencer E. Staley, Peter J. Fawcett, Gonzalo Jiménez-Moreno, R. Scott Anderson, Vera Markgraf, Erik T. Brown

(East & Sankey, 2020). Therefore, more accurate forecasting requires analysis of paleo-archives that can support interdisciplinary study of land surface processes at the critical zone system level over long timescales, that is, centuries to tens of millennia (Ashley, 2020).

This study seeks to understand the bedrock weathering and erosional consequences of climatic and related ecological changes in the high deserts, woodlands, and forests of southwestern North America (SWNA) with specific interest in episodes of abrupt warming and aridification relevant to today. To do this, we examine a lake sediment core record from Stoneman Lake (STL), Arizona (AZ), USA (2,050 m elevation; 34.78 N, 111.52 W), a small (0.63 km^2), closed-basin, montane lake that shares characteristics with the rest of the southern Colorado Plateau including a semi-arid climate, significant topographic relief, dominant southern to western aspects, and volcanic bedrock (Figure 1). The lake is situated within the lower elevational domain of the Sierran montane conifer forest, predominately *Pinus ponderosa* (ponderosa pine) with *Cupressus arizonica* (Arizona cypress), *Quercus gambelii* (Gambel's oak), *Juniperus monosperma* (one-seed juniper), and *Juglans major* (Arizona walnut) (Hasbargen, 1994). This particular stand of ponderosa pine covers 5.1 million acres along the Mogollon Rim from north-central Arizona to western New Mexico (Brown, 1982; Hanks et al., 1983) and is an important resource, having multiple uses from lumber, rangeland, and recreation to endangered species habitat and Native American practices (USDA Forest Service, 2022, https://www.fs.usda.gov/coconino). Downslope of the catchment area at approximately 2,050 m elevation is the upper limit of the pygmy conifer forest (Figure 1b) consisting of *Pinus edulis* (Colorado piñon) and several junipers (*Juniperus monosperma*, *J. deppeana*, *J. osteosperma*) intermixed with drought-tolerant shrubs (Brown, 1982). As current climate changes continue, these piñon-juniper woodlands are expected to migrate up elevation and displace portions of the ponderosa forest (Bradford et al., 2020). Understanding how past climate changes have affected this landscape is critical for resource management planning (Bradford et al., 2018) both on the Mogollon Rim and across the rest of the high plateaus of Arizona and New Mexico, where piñon-juniper woodlands and adjacent higher-elevation ponderosa pine forests occupy ∼22.2 and ∼8 million acres, respectively (Brown, 1982; Mitchell & Roberts, 1999; Pearson, 1950).

Today, mean annual temperature and precipitation (MAT and MAP) in the STL area are 7.8–10°C and 600–700 mm, respectively (Western Regional Climate Center, 2022, https://www.wrcc.dri.edu/cgi-bin/cliMAIN.pl?az3828; PRISM Climate Group, 2022, https://prism.oregonstate.edu/normals/). Cold-season (DJFM) and warm-season (JAS) precipitation accounts for around 50% and 35% of total annual precipitation, respectively, reflecting the influence of winter frontal and monsoonal precipitation (Hereford, 2007). Groundwater inputs into the lake are contingent upon recharge occurring nearby from precipitation during recent cold seasons (Blasch et al., 2006). Previous work on the lake catchment's paleo-hydrology and ecology shows lake level and local forest species composition are sensitive to global glacial-interglacial climate changes (Staley et al., 2022; Jiménez-Moreno et al., 2023). Palynology and microscopic charcoal counts of lake sediment core STL14 span multiple glacial-interglacial cycles of the Quaternary Period and show that local forest ecosystems migrate upslope and experience greater wildfire activity during warm-and-dry interglacials compared to cool-and-wet glacials (Jiménez-Moreno et al., 2023). Forest migrations have resulted in local occupations by piñon-juniper woodlands, montane pine forests, and subalpine forest communities. These changes likely affected sediment transport in the STL basin by influencing runoff and soil cohesion (Burns & Honkala, 1990; Davenport et al., 1998; Gyssels et al., 2005; MacDonald & Huffman, 2004; Pregitzer et al., 2002; Rasmussen et al., 2017; Viles, 1990).

STL and its catchment are well-characterized and have ideal characteristics for studying weathering and transport of sediments in relation to Quaternary Period climatic and ecological changes. Local bedrock is lithologically simple, comprised entirely of mid-Miocene to late Pliocene-aged alkaline olivine basalt of the Mormon Mountain Volcanic Field, a 3,500 km^2 province extending south of Flagstaff, AZ (Gust & Arculus, 1986; Holm et al., 1989). Sediment transport in the basin is clearly dominated by alluvial and colluvial processes. The basin is circular and bowl-shaped; a grass and shrub-covered apron of colluvial sediments surrounds the lake, which is encircled by steep, often cliffy, ponderosa pine-forested slopes with >40 m of local relief (Figure 1b). The rest of the catchment area drains the steep southwestern slopes of the Lake Mountain volcano (Figure 1c) and 66% of the drainage is south and west facing (from 158 to 293° azimuth) (Figure 1d). This simple basin geometry restricts spatial variability of deposition into the lake, further reducing the complexity of clastic inputs preserved in lake sediments. Furthermore, the catchment's size (3.5 km^2) and steepness (average: ∼12.6°; 50% of the area ≥10° (Figure 1e)) promote a high degree of sedimentary connectivity between the lake and surrounding hillslopes. This increases the likelihood that indicators of erosion in the lake sediments reflect the catchment's primary response

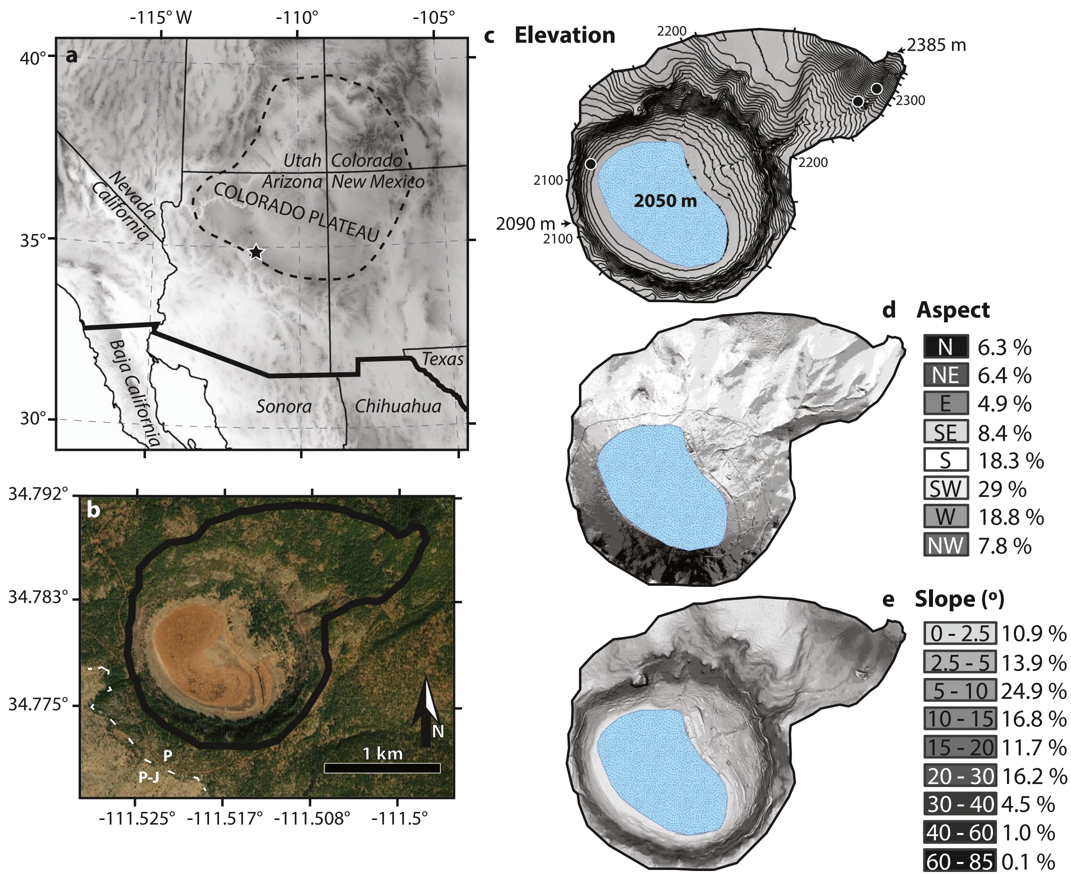

Figure 1. Setting and morphology of the Stoneman Lake (STL) catchment. (a) STL's location (star) on the Mogollon Rim, the southwestern escarpment of the Colorado Plateau. (b) Aerial image of the STL catchment (black outline). The ponderosa (P)-piñon-juniper (P–J) ecotone is at the southwest corner of the image (dashed white line). Topographic characteristics of the catchment including 5-m topographic contours (c), aspect (d), and slope (e). The locations of colluvium samples are noted by black dots in (c). Lake Mountain is in the northeast corner of the catchment.

to perturbation. Finally, the weathering products of the local basalt are easily differentiated from felsic eolian sediments, facilitating the identification, tracing, and quantification of each sediment type.

In this study, we first employ microscopic, mineralogical, and geochemical analyses of local bedrock and colluvium to investigate processes of bedrock weathering, sediment production, and erosion occurring in the modern catchment. Next, using X-ray fluorescence (XRF) scanning of core STL14, we measure elemental titanium counts—an indicator of the concentration of the conservative and locally-sourced ilmenite ($FeTiO_3$)—to trace catchment erosion rates over the last 250 kyr. The length of the core record is significant. Few regional paleorecords extend beyond the Last Glacial, which began around 75 ka at the Marine Isotope Stage (MIS) 5 to 4 transition, and therefore fail to capture the effects of the penultimate deglaciation at the MIS 6 to 5 transition and subsequent interglacial conditions of MIS 5. We then correlate catchment erosion (Ti counts) to changes in climate, vegetation, and fire activity through time. Also, because eolian dust is readily identifiable and comprises a significant portion of sediment within the lake catchment, we can simultaneously characterize its introduction to this landscape. Finally, we explore how connections between climate, biology, and erosion inform predictions for modern subalpine to montane pine forests, threatened today by anthropogenic changes like increased tree mortality, forest fire, and displacement by drought-adapted plant communities.

2. Materials and Methods

In this study, we characterize bedrock, colluvium, and lake sediments from the STL catchment using quantitative X-ray diffraction (qXRD), scanning electron microscopy (SEM), and quantitative and core scanning

XRF geochemistry. Mineralogy and geochemistry of the modern catchment inform interpretations of sedimentary processes in lacustrine core data. Combined with previously published stratigraphies of paleoclimate and paleoecology, these data demonstrate how climate, vegetation, and forest fire activity affect sedimentary processes in this basin.

2.1. Core Retrieval, Age Model, and Earlier Work

Two sediment cores were retrieved from the STL depocenter in October 2014 using a truck-mounted percussion coring apparatus. Their composite, core STL14, contains a continuous ~80-m archive of the last ~1.3 Ma. A complete account of the cores' retrieval, initial description, composite scale construction, lithofacies analysis, and initial age model can be found in Staley et al. (2022). The age model includes 10 radiocarbon analyses spanning the late Pleistocene and Holocene, tephrochronology, and a well-justified correlation of abrupt deep-to-shallow facies transitions to glacial terminations. Here, we introduce further age control by correlating STL14 stratigraphy with an overlapping core containing seven additional Holocene-aged radiocarbon dates (Hasbargen, 1994) and perform Bayesian age modeling to assess uncertainty (Blaauw & Christen, 2012) (Figures S1 and S2, Table S1 in Supporting Information S1). Sedimentary facies and palynology demonstrate the sensitivity of the lake and surrounding ecosystems to climate changes at glacial to millennial timescales (Jiménez-Moreno et al., 2023; Staley et al., 2022). In general, glacial periods are colder and wetter. This is shown by sedimentary facies consistent with a deeper lake combined with an increase in pollen from subalpine and montane conifer taxa like *Abies concolor* and *A. lasiocarpa* (white and subalpine fir), *Pseudotsuga menziesii* (Douglas fir), and *Picea engelmannii* (Englemann spruce) that currently grow predominantly at elevations ~1,000 m above the catchment. Interglacials are warmer and drier overall, indicated by an increase in pollen from montane pines (species comprising the montane pine group could include ponderosa pine, *Pinus strobiformis* (southwestern white pine), *P. flexilis* (limber pine), and perhaps even *P. contorta* (lodgepole pine); macrofossil analysis is required to differentiate them further) and thermophilous tree taxa (piñon, juniper, and oak) and sedimentary facies consistent with a shallower lake. Paleoclimatic interpretations agree with those from other local and nearby records (Anderson et al., 2000; Hasbargen, 1994; Hereford & Amoroso, 2020).

2.2. Sampling

This study examines the upper ~13 m of core STL14, which contains clastic-dominated lacustrine and palustrine sediments of the last ~250 kyr. Lake sediment samples (n = 28) were obtained for qXRD analysis at ~50-cm-resolution referenced to the depth scale measured in meters composite below the lake floor (mcblf). This data set has the coarsest stratigraphic resolution of this study, corresponding to an 8-kyr median sample resolution (Holocene: 2.6-kyr; Last Glacial: 7-kyr; MIS 5: 8.4-kyr; MIS 6: 15.8-kyr; MIS 7: 14.8-kyr). Seven basalt cobbles were gathered from the ground surface near their outcrop source with at least one sample from each of the five most aerially extensive units found in the catchment (Figure S3a in Supporting Information S1). The unweathered interior of cobble samples defines the local bedrock parent material; bedrock mineralogy is nearly homogenous catchment-wide (Dohm, 1995, Text S2 in Supporting Information S1). Three samples of the fine-grained fraction of colluvium were gathered from ~10 to 20 cm depth at +252, +207, and +8 m relative to the modern lake floor (Figure 1c) to observe downslope changes in sediment composition. Images of sample pit profiles can be found in Figure S3c in Supporting Information S1. These samples are representative of the two main colluvial soil environments present within the catchment: (a) hillslopes with Typic-to-Lithic Argiustolls in the Sponseller, Cabezon, and Brolliar series that grade into (b) the alluvial/colluvial apron around the lake with Vertic Argiustolls in the Friana series (Williams & Anderson, 1967). Samples were sieved into their fine fractions (<150 μm) to better isolate signals of chemical weathering, pedogenesis, and dust accumulation.

2.3. Analyses

2.3.1. qXRD

Mineralogical analysis of local bedrock (n = 1), colluvium (n = 3), and lake sediments (n = 28) was performed on a Rigaku SmartLab at the University of New Mexico's X-Ray Diffraction Laboratory. Quantitative analysis was conducted on the diffractograms using whole pattern fitting with Rietveld refinement (Post & Bish, 1989; Rietveld, 1969). Information about the sample preparation, refinement procedures, and diffractograms can be

Journal of Geophysical Research: Earth Surface

10.1029/2023JF007266

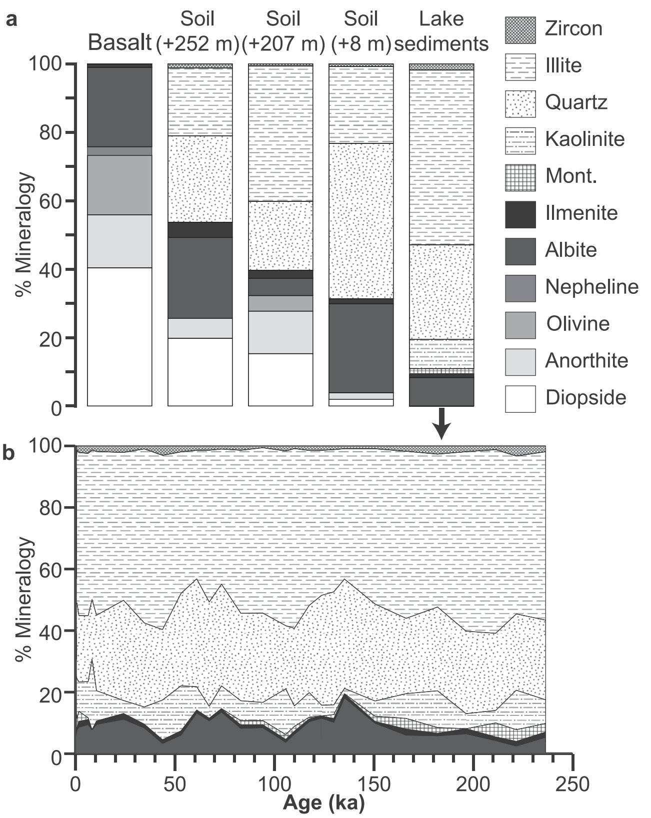

Figure 2. (a) Mineralogical comparison of catchment materials. Eolian content in colluvium (quartz and illite) increases moving closer to the lake in elevation. (b) Quantitative X-ray diffraction analyses ($n = 28$) of lake sediment spanning the last ~240 kyr.

found in Text S3 and Figure S4 in Supporting Information S1 and Data Set S1).

2.3.2. Geochemistry

Quantitative elemental analysis of each bedrock ($n = 7$) and colluvial ($n = 3$) sample was carried out on a Rigaku Primus VI XRF machine at the University of New Mexico's Analytical Geochemistry Laboratory. Elemental analysis of core sediments took place at the University of Minnesota Duluth using an ITRAX XRF core scanner operated by the Continental Scientific Drilling Facility's XRF Laboratory. Core scanning results are not purely quantitative but they can be compared to quantitative data sets using element ratios. Although a wide range of elements are reported, we focus on Al, Si, K, Ca, Ti, Fe, Rb, Sr, and Zr, all of which are reliably detected and measured using the core scanning technique. Conservative lithophile elements such as Ti, Rb, and Zr are often used as tracers of clastic sediments in the surface environment because of their immobility during chemical weathering (e.g., Chen et al., 2006; Haug et al., 2003; Muhs & Benedict, 2006). We used Ti to trace local sedimentation and Rb and Zr to trace eolian sedimentation in core sediments. Details of sample processing, analytical parameters, and composite XRF data are in Text S4 in Supporting Information S1 and Data Set S2.

2.3.3. Scanning Electron Microscopy

Further textural and mineralogical analyses of four of the bedrock samples and their weathering rinds were performed on a Vega 3 Tescan Scanning Electron Microscope at the University of New Mexico's Electron Microbeam Facility. Backscattered electron imagery and energy dispersive X-ray spectroscopy (EDS) were used to characterize the geochemical and mineralogical changes in the weathering rinds. Information about sample processing, analytical parameters and SEM imagery and EDS results are detailed in Text S5 in Supporting Information S1 and Data Set S3.

3. Results

3.1. Mineralogy

qXRD analysis shows that local basalt is 40% diopside, 39% plagioclase (23% albite and 16% anorthite), 17% olivine, 3% nepheline, and 1% ilmenite (Figure 2a; Table 1), in agreement with earlier analyses (Dohm, 1995; Gust & Arculus, 1986; McCabe, 1971). In contrast, lake sediments contain a more felsic mineral assemblage comprising 51% illite, 28% quartz, 9% kaolinite, 8% albite, 2% montmorillonite, 2% zircon, and 1% ilmenite over the last ~240 ka (Figures 2a and 2b; Table 1). Apart from changes in the presence of trace amounts of smectite, this mineral assemblage remains consistent (Figure 2b). A more subtle stratigraphic variation is not precluded given the coarse sample resolution and inherent uncertainties in the qXRD method (Moore & Reynolds, 1997; Raven & Self, 2017). The composition of the <150-μm-fraction of catchment colluvium is intermediate to those of lake sediments and bedrock, averaging 27% illite, 30% quartz, 18% albite, 7% anorthite, 12% diopside, 3% ilmenite, 2% olivine, and 1% zircon (Figure 2a; Table 1). The lake's colluvial apron contains a smaller fraction of mafic minerals and a greater fraction of quartz and illite than colluvium found higher in elevation in the catchment (Figure 2a).

We can disregard the presence of calcite, corundum, and weddellite in lake sediments (Table 1). Carbonates are mostly below detection limits, in agreement with low abundances observed in smear slides (Staley, 2018). Calcite is present below 10.68 mcblf, likely a result of diffuse diagenetic accumulations associated with shallow diagenesis rather than primary authigenic precipitation (Staley et al., 2022). Detection of corundum and weddellite seems to be the result of sample preparation techniques.

BSE imagery and EDS analysis reveal finer-scale textural and mineralogical features of STL basalts (Figure 3; Data Set S3), consistent with qXRD results. Unweathered basalt contains abundant subhedral clinopyroxene

Table 1
Quantitative X-Ray Diffraction Results for Stoneman Lake Bedrock, Colluvium, and Lake Sediments

Sample ID	Core depth (cmcblf)	Age (ka)	R[b] (%)	E[c] (%)	Diopside	Anorthite	Albite	Olivine	Nepheline
Basalt									
STLB-19-1	**na**	**m.Mio-l.Plio**	**2.93**	**1.2**	**40.4**	**15.5**	**23.2**	**17.4**	**2.5**
McCabe (1971) and Dohm (1995) [d]	**na**	**m.Mio-l.Plio**	**na**	**na**	**33**[a]	**40**[e]		**16.0**	**0.0**
Gust and Arculus (1986) [e]	**na**	**m.Mio-l.Plio**	**na**	**na**	**17.5**	**28.7**	**21.0**	**17.0**	**3.5**
Colluvium									
STL21-S-1-13 + 25	na	~Modern	4.13	1.19	1.9	2.0	26.0	0.0	0.0
STL21-S-2-10	**na**	**~Modern**	**3.32**	**1.15**	**19.8**	**5.8**	**23.6**	**0.0**	**0.0**
STL21-S-3-10	na	~Modern	3.41	1.13	15.3	12.4	5.1	4.6	0.0
Average					12.3	6.7	18.2	1.5	0.0
Lake sediment									
STL-STL14-1B-1C-1-W-10	**10**	**0.12**	**3.76**	**1.16**	**0.0**	**0.0**	**4.9**	**0.0**	**0.0**
STL-STL14-1B-1C-1-W-50	**50**	**0.78**	**3.78**	**1.18**	**0.0**	**0.0**	**6.4**	**0.0**	**0.0**
STL-STL14-1B-1C-1-W-100	100	1.73	3.63	1.15	0.0	0.0	8.2	0.0	0.0
STL-STL14-1B-2C-1-W-10	147	6.38	4.09	1.16	0.0	0.0	9.0	0.0	0.0
STL-STL14-1B-2C-1-W-60	176	8.33	3.64	1.18	0.0	0.0	5.3	0.0	0.0
STL-STL14-1A-3C-1-W-50	242	10.60	3.11	1.14	0.0	0.0	7.3	0.0	0.0
STL-STL14-1A-3C-1-W-100	292	24.2	3.5	1.2	0.0	0.0	8.9	0.0	0.0
STL-STL14-1B-3C-1-W-50	344	34.6	3.62	1.17	0.0	0.0	7.2	0.0	0.0
STL-STL14-1B-3C-1-W-100	394	43.8	3.88	1.16	0.0	0.0	2.7	0.0	0.0
STL-STL14-1B-3C-1-W-150	444	53.1	3.74	1.17	0.0	0.0	5.6	0.0	0.0
STL-STL14-1B-4C-1-W-50	501.5	61.0	3.91	1.19	0.0	0.0	10.8	0.0	0.0
STL-STL14-1B-4C-1-W-100	551.5	67.2	3.92	1.18	0.0	0.0	9.2	0.0	0.0
STL-STL14-1B-4C-1-W-150	601.5	73.4	4.16	1.19	0.0	0.0	12.5	0.0	0.0
STL-STL14-1B-5C-1-W-50	655	83.1	4.16	1.16	0.0	0.0	7.9	0.0	0.0
STL-STL14-1B-5C-1-W-100	705	94.2	4.14	1.16	0.0	0.0	8.3	0.0	0.0
STL-STL14-1B-5C-1-W-150	755	105.7	3.82	1.14	0.0	0.0	3.4	0.0	0.0
STL-STL14-1B-6C-1-W-0	779.5	110.1	4.17	1.15	0.0	0.0	6.2	0.0	0.0
STL-STL14-1B-6C-1-W-50	829.5	117.5	3.97	1.16	0.0	0.0	10.0	0.0	0.0
STL-STL14-1B-6C-1-W-100	879.5	123.7	4.3	1.17	0.0	0.0	11.1	0.0	0.0
STL-STL14-1B-6C-1-W-150	929.5	129.9	4.15	1.17	0.0	0.0	9.9	0.0	0.0
STL-STL14-1B-7C-1-W-50	968.5	135.2	4.34	1.17	0.0	0.0	17.9	0.0	0.0
STL-STL14-1B-7C-1-W-100	1,018.5	150.6	4.11	1.17	0.0	0.0	9.3	0.0	0.0
STL-STL14-1B-7C-1-W-150	1,068.5	166.2	3.62	1.16	0.0	0.0	5.4	0.0	0.0
STL-STL14-1B-8C-1-W-50	1,119	182.0	3.75	1.16	0.0	0.0	4.7	0.0	0.0
STL-STL14-1B-8C-1-W-100	1,169	196.4	4.02	1.21	0.0	0.0	6.1	0.0	0.0
STL-STL14-1B-8C-1-W-150	1,219	211.3	4.04	1.14	0.0	0.0	3.9	0.0	0.0
STL-STL14-1B-9C-1-W-50	1,252.5	221.6	4.16	1.14	0.0	0.0	2.2	0.0	0.0
STL-STL14-1B-9C-1-W-100	1,302.5	236.4	4.07	1.13	0.0	0.0	5.0	0.0	0.0
Average					0.0	0.0	7.5	0.0	0.0
					Diopside	Anorthite	Albite	Olivine	Nepheline
Average − [corundum + weddellite + calcite]					**0.0**	**0.0**	**8.4**	**0.0**	**0.0**

Note. Bold values indicate emphasis

[a]Calculated from whole pattern fitting with Reitveld refinement software Materials Jade. [b]*R* is the residual of least-squares refinement scaled by weighted intensities. [c]*E* is the expected *R*-factor. [d]Both authors use modal estimates, identify the diopside as augite and clinopyroxene, respectively, and combine plagioclases into a single category. [e]CIPW normative mineralogy.

Percent abundance[a]											
Orthoclase	Magnetite	Ilmenite	Apatite	Montmorillonite	Zircon	Kaolinite	Quartz	Illite	Corundum	Weddelite	Calcite
0.0	**0.0**	**1.0**	**0.0**	**0.0**	**0.0**	**0.0**	**0.0**	**0.0**	**0.0**	**0.0**	**0.0**
0.0	**8.0**	**0.0**	**0.0**	**0.0**	**0.0**	**0.0**	**1.0**	**0.0**	**0.0**	**0.0**	**0.0**
5.8	**2.8**	**2.7**	**0.7**	**0.0**	**0.0**	**0.0**	**0.0**	**0.0**	**0.0**	**0.0**	**0.0**
0.0	0.0	1.5	0.0	0.0	0.8	0.0	45.4	22.4	0.0	0.0	0.0
0.0	**0.0**	**4.5**	**0.0**	**0.0**	**1.2**	**0.0**	**25.3**	**19.8**	**0.0**	**0.0**	**0.0**
0.0	0.0	2.3	0.0	0.0	0.6	0.0	20.1	39.6	0.0	0.0	0.0
0.0	0.0	2.8	0.0	0.0	0.9	0.0	30.3	27.3	0.0	0.0	0.0
0.0	**0.0**	**0.5**	**0.0**	**7.4**	**6.2**	**9.7**	**20.1**	**38.0**	**11.4**	**1.8**	**0.0**
0.0	**0.0**	**0.7**	**0.0**	**2.5**	**1.1**	**10.7**	**20.5**	**41.4**	**8.3**	**8.4**	**0.0**
0.0	0.0	1.8	0.0	3.1	2.0	9.1	20.4	50.1	4.6	0.8	0.0
0.0	0.0	1.6	0.0	0.5	2.3	11.2	20.4	50.3	1.8	2.9	0.0
0.0	0.0	0.0	0.0	0.0	0.9	15.7	13.4	33.4	14.8	16.5	0.0
0.0	0.0	0.8	0.0	0.0	1.4	7.5	18.7	40.6	20.1	3.6	0.0
0.0	0.0	1.5	0.0	0.0	1.7	3.3	25.8	38.1	20.8	0.0	0.0
0.0	0.0	1.0	0.0	0.0	0.8	4.8	23.3	48.2	14.8	0.0	0.0
0.0	0.0	0.9	0.0	0.0	2.4	10.4	18.3	45.3	20.0	0.0	0.0
0.0	0.0	1.3	0.0	0.0	1.8	13.5	27.7	42.4	7.7	0.0	0.0
0.0	0.0	0.8	0.0	0.0	1.2	6.2	28.5	34.0	18.6	0.0	0.0
0.0	0.0	0.7	0.0	0.0	1.2	3.4	29.2	42.5	13.8	0.0	0.0
0.0	0.0	0.8	0.0	0.2	0.9	6.8	30.6	40.6	7.5	0.0	0.0
0.0	0.0	1.0	0.0	1.4	1.3	6.2	27.2	50.8	3.5	0.7	0.0
0.0	0.0	0.9	0.0	1.4	0.6	5.8	28.4	52.7	2.0	0.0	0.0
0.0	0.0	0.8	0.0	1.5	1.5	13.4	18.5	51.1	6.8	3.2	0.0
0.0	0.0	1.0	0.0	1.6	0.8	6.5	24.8	57.5	1.0	0.6	0.0
0.0	0.0	0.8	0.0	0.6	1.4	7.7	27.2	48.3	4.1	0.0	0.0
0.0	0.0	0.7	0.0	0.0	1.4	3.4	34.2	45.2	4.1	0.0	0.0
0.0	0.0	1.1	0.0	1.3	1.2	3.1	35.6	44.8	3.1	0.0	0.0
0.0	0.0	1.1	0.0	0.2	0.9	1.7	34.9	41.6	1.7	0.0	0.0
0.0	0.0	0.5	0.0	1.6	0.9	4.6	29.5	47.2	6.5	0.0	0.0
0.0	0.0	1.8	0.0	3.1	1.5	7.2	21.8	48.3	8.2	0.0	2.8
0.0	0.0	0.7	0.0	1.5	2.1	9.6	22.0	40.1	7.6	0.0	11.6
0.0	0.0	1.5	0.0	0.0	1.8	4.6	25.1	54.7	4.6	0.0	1.5
0.0	0.0	1.1	0.0	4.2	1.1	3.7	23.1	54.9	3.7	0.0	4.3
0.0	0.0	1.3	0.0	3.4	2.9	11.4	22.0	45.5	7.0	0.0	4.4
0.0	0.0	1.6	0.0	2.6	1.7	7.2	24.1	51.0	5.4	0.0	1.4
0.0	0.0	1.0	0.0	1.4	1.6	7.4	24.8	45.7	8.3	1.4	0.9
Ilmenite	Montmorillonite	Zircon	Kaolinite	Quartz	Illite						
1.1	**1.5**	**1.8**	**8.3**	**27.8**	**51.1**						

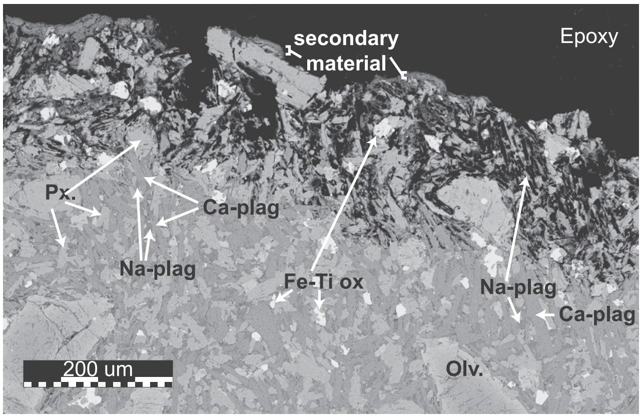

Figure 3. Scanning electron microscopy image of a basalt weathering rind in cross-section. Mineral phases in order of brightness: Fe-Ti oxides and apatite > olivine > diopside > anorthite > albite.

(diopside) and well-defined calcic plagioclase (anorthite) laths. Sodic plagioclase (albite), the darkest phase in BSE images, is slightly less abundant and poikilitic, filling in spaces between other crystals. Euhedral, sometimes porphyritic, magnesium-rich olivine is the next most abundant mineral. Ilmenite is a common accessory mineral while magnetite and apatite can be found in trace quantities.

Weathering rind thickness ranges from roughly 200–400 μm in the four samples analyzed under SEM. Vesicular basalts have deeper weathering profiles and more diffuse boundaries with unweathered cores. Void space is lath-shaped, indicating dissolution of anorthite (Figure 3; Data Set S3; e.g., Navarre-Sitchler et al., 2009, 2011). EDS analyses indicate albite remains abundant in the rind, agreeing with the poikilitic texture of most remaining minerals. Ilmenite, magnetite, and some diopside are also present. Secondary mineralization is limited to the outer 10–20 μm, ranges from globular to laminated in appearance and is largely composed of aluminum, silicon, and oxygen, with minor amounts of potassium, iron, magnesium, calcium, and titanium, consistent with the chemistry of a 2:1 clay (Figure 3; Data Set S3). Without further analyses, we cannot determine whether this secondary material is amorphous or crystalline, though it is likely some combination of clay minerals, short-range order materials including allophane that act as clay precursors (Colman, 1982; Eggleton et al., 1987), and various iron oxides and oxyhydroxides (e.g., Heckman & Rasmussen, 2011).

3.2. Geochemistry

Colluvial fine-fraction and bedrock geochemistries are provided in Table 2 and Table S2 in Supporting Information S1. The normalized concentration of cations in colluvium ($\mathrm{T}_{i,j}$, Figure 4a) accounts for volume changes and relative loss or gain of elements (Equation 1, Brimhall & Dietrich, 1987) and illustrates processes in the critical zone.

$$\mathrm{T}_{i,j} = \frac{C_{j,w}}{C_{j,p}} \frac{C_{i,p}}{C_{i,w}} - 1 \tag{1}$$

C represents the concentration of immobile (i) or mobile (j) elements in weathered (w) or parent (p) material. We use Ti as the locally sourced and immobile cation, i, to normalize the concentrations of other elements. The concentration of an element in weathered material is identical to that of the parent when $T = 0$. When an element is lost to dissolution or biological uptake, $T < 0$. Complete loss of an element is indicated by $T = -1$. When an element is enriched, $T > 0$. The concentrations of conservative elements Al, Si, Ti, and Fe have T values near 0, indicating that they have undergone little modification by modern weathering processes in the shallow subsurface. Conversely, Na, Mg, P, Ca, and Sr have negative T values indicating depletion by chemical dissolution and/or biological uptake (Jobbágy & Jackson, 2001). K, Rb, and Zr have positive T values, suggesting their addition to colluvium by eolian dust deposition, or potentially in the case of K, biological transfer. In lake sediments, conservative lithophile elements associated with clastic sediment (Al, Si, Ti, Fe, K, Rb, and Zr) are positively correlated (Figure 4b). More chemically mobile elements Ca and Sr exhibit weak to negative correlations with these conservative elements, suggesting that their concentration in lake sediments, like in colluvium, is controlled by chemical weathering. Principal component analysis of core scan data likewise partitions calcium from other lithophile elements (Figure 4c). Principal component (PC) 1 accounts for 63% of the data set's variability and has highly positive factor loadings for all elements except calcium. PC2 accounts for ~21% of the data set's variability and captures the division between conservative (Al, Si, Ti, and Fe) and enriched elements (K, Rb, and Zr), as seen in Figure 4a. See Text S6 and Figure S5 in Supporting Information S1 for more information related to this PCA.

Comparing plots of XRF core scans spanning the last 250 kyr supports these statistical relationships with all elements but Ca following similar trends (Figure 5). Elements associated with clastic sediment correlate with bulk density and exhibit weak anticorrelation with total organic carbon (TOC), an indicator of non-clastic content. Relatively low TOC values overall suggest that the amount and composition of clastic influx controls

10.1029/2023JF007266

Table 2
Major Element Oxide (Weight %) and Selected Minor Element Concentration (ppm) Geochemistry of Stoneman Lake Catchment Bedrock and Colluvium

Sample	Description	Basalt unit[a]	Latitude	Longitude	Elev. (m)	SiO_2	TiO_2	Al_2O_3	Fe_2O_3	MnO	MgO	CaO	Na_2O	K_2O	P_2O_5	Sr	Rb	Zr
Colluvium																		
STL21-S-1	**13–25 cm depth in colluvial apron**	**Tslb1**	**34.782**	**−111.524**	**2,056**	**65.3**	**1.41**	**18.1**	**6.7**	**0.10**	**1.2**	**2.7**	**1.4**	**2.5**	**0.26**	**324**	**104**	**439**
STL21-S-2	10 cm depth in hillslope colluvium	Tys	34.787	−111.500	2,300	55.0	1.95	17.6	11.7	0.24	2.6	5.8	1.6	2.7	0.29	565	100	364
STL21-S-3	10 cm depth in hillslope colluvium	Tys	34.786	−111.501	2,255	52.0	2.25	23.5	12.6	0.23	2.4	3.2	1.0	2.0	0.36	453	139	341
Average						**57.4**	**1.87**	**19.7**	**10.3**	**0.19**	**2.1**	**3.9**	**1.3**	**2.4**	**0.30**	**447**	**114**	**381**
σ						**7.0**	**0.43**	**3.3**	**3.2**	**0.08**	**0.8**	**1.7**	**0.3**	**0.4**	**0.05**	**121**	**22**	**51**
$\tau_{Ti,j}$						**0.08**	**0.00**	**−0.03**	**−0.22**	**−0.20**	**−0.70**	**−0.68**	**−0.68**	**0.58**	**−0.64**	**−0.71**	**4.51**	**1.07**
$\sigma(\tau_{Ti,j})$						**0.33**	**0.43**	**0.35**	**0.45**	**0.53**	**0.57**	**0.55**	**0.42**	**0.50**	**0.45**	**0.51**	**0.50**	**0.43**
Basalt																		
[b, c]**STL19-B-1**	**Alkali olivine basalt**	**Tsb**	**34.772**	**−111.511**	**2,141**	**45.4**	**1.06**	**16.5**	**10.4**	**0.18**	**8.8**	**12.1**	**3.2**	**0.9**	**0.87**	**1,260**	**18**	**121**
[c]STL19-B-2	Alkali olivine basalt	Tlb	34.770	−111.519	2,117	48.1	1.98	18.4	11.2	0.23	4.3	8.6	3.9	1.9	0.86	1,471	24	230
[c]STL19-B-3	Alkali olivine basalt	Tslb1	34.780	−111.526	2,101	43.1	1.79	18.0	12.3	0.24	6.7	12.1	3.2	1.1	0.86	1,691	nd	184
[c]STL19-B-4	Alkali olivine basalt	Tslb2	34.779	−111.525	2,099	42.9	1.72	17.9	12.1	0.21	7.6	12.1	3.2	1.0	0.74	1,454	nd	153
STL21-B-1	Alkali olivine basalt	Tslb1	34.784	−111.521	2,063	46.0	1.36	18.6	13.5	0.21	5.1	10.2	3.7	0.7	0.29	463	nd	91
STL21-B-2	Alkali olivine basalt	Tys	34.788	−111.498	2,371	49.7	1.57	17.2	9.4	0.17	5.3	9.2	4.4	1.7	0.75	1,421	21	170
STL21-B-3	Alkali olivine basalt	Tys	34.787	−111.500	2,300	48.7	1.91	17.6	11.3	0.21	3.7	9.6	3.8	1.9	0.81	1,556	9	175
Average						**46.3**	**1.63**	**17.7**	**11.5**	**0.21**	**5.9**	**10.6**	**3.6**	**1.3**	**0.74**	**1,331**	**18**	**160**
σ						**2.7**	**0.33**	**0.7**	**1.3**	**0.02**	**1.8**	**1.5**	**0.5**	**0.5**	**0.21**	**404**	**6**	**45**

Note. Bold values indicate emphasis
[a]Units of Dohm (1995), Text S2, Figure S3 in Supporting Information S1 [b]Bedrock sample analyzed by XRD. [c]Bedrock sample analyzed by SEM.

10.1029/2023JF007266

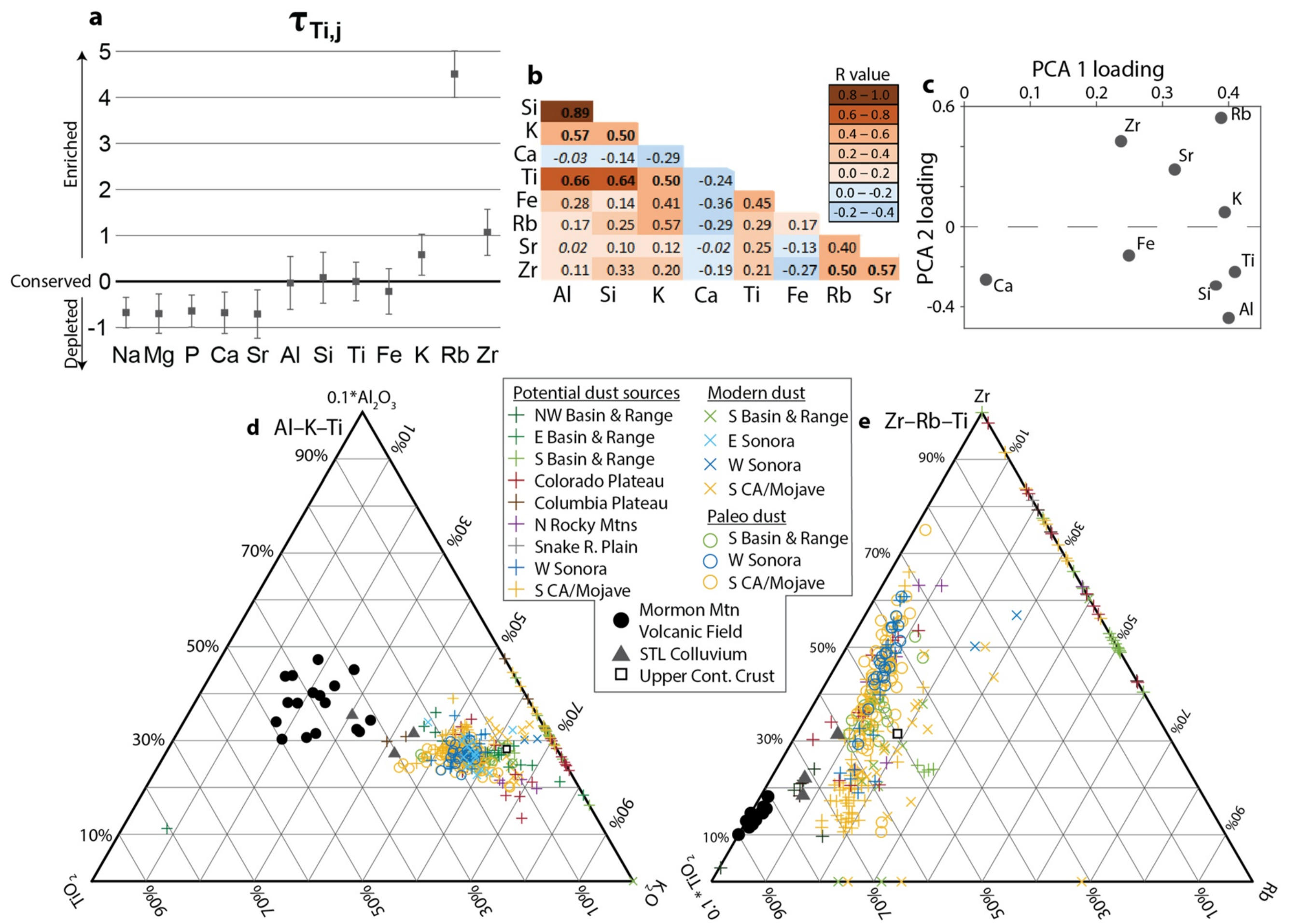

Figure 4. Geochemistry of Stoneman Lake bedrock, colluvium, and lake sediments. (a) Normalized average cation concentration ($\tau_{Ti,j}$) of colluvial fine-fraction (<150 μm, $n = 3$) compared to catchment bedrock ($n = 7$) with 1σ uncertainty. (b) Correlation coefficients of selected elements in X-ray fluorescence (XRF) core scans of lake sediments. Bold numbers correspond to R-values > 0.50. Italics denotes an insignificant correlation (p values > 0.05). (c) Loadings of the first two principal components in an analysis of XRF lake sediment core scans. (d) Geochemical comparison of catchment bedrock, colluvium, and regional dusts in Al-K-Ti space indicating a mixture of local and eolian inputs to catchment sediments. Additional bedrock values for the Mormon Mountain Volcanic Field are provided by Gust and Arculus (1986) and Rudzitis et al. (2016). Values for dust-associated materials from southwestern North America include (1) the bulk oxide geochemistry of modern dust fall samples from Tempe, Arizona (E. Sonora, Péwé et al., 1981), (2) major-to-trace element geochemistry of paleo-dust (vesicular (Av or V) soil horizons) and modern dust fall in the Southern Basin & Range, Western Sonora, and Southern California-Mojave regions (Reheis et al., 2009; Sweeney et al., 2013), and (3) geochemistries of potential dust sources throughout the American West (Aarons et al., 2017; Sweeney et al., 2013). The average chemistry of the upper continental crust (Taylor et al., 1983) is also included. Panel (e) is the same as panel (d) but in Zr-Rb-Ti space.

sediment composition rather than organic matter production and preservation. High TOC values during the Early Holocene and possibly MIS 4 could, however, cloud interpretations of clastic influx during these times (Figure 5). Mn/Fe, an indicator of redox conditions in the sediment (Davison, 1993; Makri et al., 2021; Naeher et al., 2013) trends to zero deeper in the core indicating reducing conditions (Figure 5). This supports the conclusion of Staley et al. (2022)—based on observations of low TOC, green sediment coloration, and secondary calcite precipitation—that reducing conditions below ∼8 mcblf resulted from the consumption of oxidizing agents during the remineralization of buried organic material.

4. Discussion

Local weathering, erosion, and eolian accumulation influence the composition of colluvial and lacustrine sediments in the STL catchment. We first investigate how local basalts weather and become sediment by looking at mineralogical changes in weathering rinds and physical and geochemical characteristics of colluvial sediments.

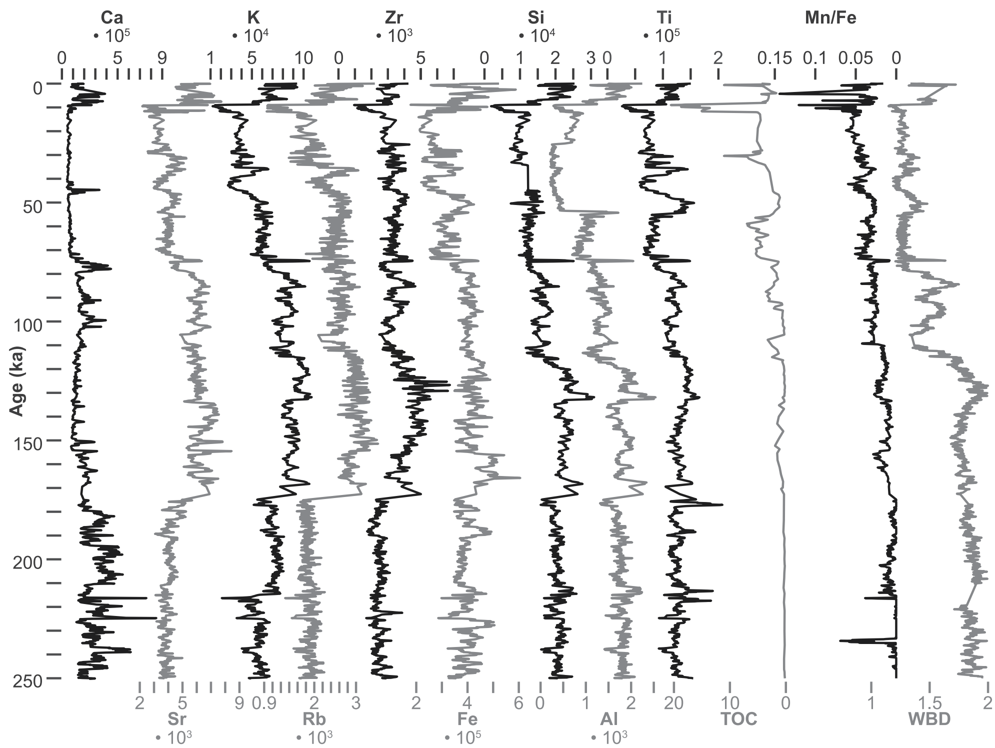

Figure 5. Geochemical and physical analyses of core STL14. Counts per second of elements calcium (Ca), strontium (Sr), potassium (K), rubidium (Rb), zirconium (Zr), iron (Fe), silicon (Si), aluminum (Al), and titanium (Ti). The manganese to iron ratio (Mn/Fe) is an indicator of redox conditions in the sediment column. Other compositional indicators include total organic carbon and wet bulk density (Staley et al., 2022).

Next, we use titanium counts in lake core sediments as an indicator of catchment erosion rates, an approach validated by ilmenite's conservative behavior in bedrock, colluvium, and lake sediment. Next, we correlate titanium and smectite/kaolinite (potentially an indicator of erosion depth) to previous paleoenvironmental interpretations derived from palynology and lithology. By exploring relationships between erosion and environment, we predict long-term responses of similar environments to anthropogenic climate change. We conclude by discussing the role of dust in this environment, how it has changed over time, and factors affecting the amount and character of dust inputs.

4.1. Basalt Weathering and Colluvium Production

Chemical and physical weathering combine to degrade catchment basalts into both fine and coarse particles, indicated by the mineralogical, geochemical, and physical characteristics of weathering rinds and colluvium within the catchment. In weathering rinds, bedrock is affected by various environmental forces that cause it to degrade, become susceptible to physical removal (erosion), and ultimately contribute much of the clay-to-silt-sized material found in colluvium. Our microscopic analyses show chemical dissolution of primary minerals like Ca-plagioclase and olivine creates void space in the inner rind (Figure 3). Dissolution exposes the remaining mineral grains to further dissolution, weakening the rock's internal structure (Navarre-Sitchler et al., 2011). Mineral grains resisting dissolution are exposed to external erosive forces probably dominated by colluvial abrasion given the predominance of colluvium in the catchment. The presence of coarse pebble-to-cobble-sized bedrock clasts in colluvium (Figure S3c in Supporting Information S1) suggests that dissolution likely works in tandem with subcritical cracking, the primary mechanism for physical degradation of rocks at Earth's surface driven by climate-dependent chemo-physical reactions that propagate crack tips (Eppes & Keanini, 2017). Mineral transformations into secondary materials such as clay (Figure 3) may also promote the degradation of bedrock (Nara et al., 2011). While frost weathering may not contribute significantly to coarse sediment production during warmer interglacials, rates were likely much higher during cold glacial episodes of the past (Marshall et al., 2021).

4.2. Chemical Weathering of Colluvium

Once bedrock is transformed into colluvium, significant mineralogical and geochemical changes continue to occur as it is transported downslope in response to continued chemical weathering and inputs of eolian material. Complete chemical dissolution of olivine appears to occur almost entirely within the weathering rind (Figures 2a and 3). Anorthite and diopside also completely dissolve before deposition in STL although they appear to be slightly more resistant given their presence in colluvium (Figures 2a and 3). Albite and ilmenite are the only locally sourced minerals that avoid total chemical dissolution in both the rind and soil environments (Figures 2 and 3), in agreement with previous work noting their resistance (Blum & Stillings, 1995; Brimhall & Dietrich, 1987; Goldich, 1938; Milnes & Fitzpatrick, 1989). Basaltic mineral susceptibility to chemical weathering at STL can be ranked as follows: Olivine > anorthite > diopside > albite > Fe-Ti oxides. Relative mineral susceptibility is consistent through time because local mineral proportions in lake sediment do not change significantly (Figure 2b). Elemental compositions in the bedrock-to-colluvium-to-lake sediment continuum agree with mineralogical trends in chemical weathering resistance. Al, Si, Ti, and Fe are all fairly insoluble elements associated with albite ($NaAlSi_3O_8$) and ilmenite ($FeTiO_3$), whereas elements including Na, Mg, and Ca are all fairly soluble and associated with minerals like nepheline ($Na_3KAl_4Si_4O_{16}$), anorthite ($CaAl_2Si_2O_8$), diopside ($MgCaSi_2O_6$), and olivine ($MgSiO_4$) (Figure 4). Because titanium concentration in sediments is most likely controlled by the concentration of locally-derived and conservative-behaving ilmenite, we will use Ti counts in core sediments to trace sediment transport into the lake through time.

4.3. Clay Minerals

In addition to Ti counts, stratigraphic variability of clay mineral assemblage in lake sediments may be important for understanding erosion patterns in the STL catchment, specifically whether sediment transport is occurring via mainly hillslope creep or by more active alluvial/colluvial processes like gullying. Past work has shown that smectite and kaolinite are common weathering products of basalt, even in drier environments (Birkeland, 1999; Eggleton et al., 1987; Vingiani et al., 2004). Here, regression analysis relating the sum of kaolinite and smectite to that of quartz and illite (dust minerals) in lake sediments shows a strongly negative relationship (−0.7 slope, $r^2 = 0.64$), suggesting that these clays are local rather than eolian (e.g., Claquin et al., 1999; Lawrence et al., 2010; Reheis & Kihl, 1995).

Nearby analyses—in addition to finding similar mineral compositions, chemical weathering susceptibilities, and eolian dust additions to Holocene-aged basaltic soils—indicate that kaolinite is found in greater abundances in surface horizons, whereas smectite is concentrated deeper in the subsurface (Heckman & Rasmussen, 2011). While neither clay was observed in colluvium samples at STL, this does not necessarily preclude their local origin—kaolinite and smectite content may be below the detection limit of our XRD methodology. If these clay minerals are indeed products of local weathering, their relative abundances through time in lake sediments could suggest changes in the intensity of erosion within the catchment: kaolinite indicating primarily shallow sediment transport by soil creep, and smectite indicating active gullying that is tapping sediment from Bt horizons deeper in the soil profile. Therefore, the ratio of smectite to kaolinite (Sm/Kao) (Figure 6h) may reflect the intensity (depth) of erosion, with lower values indicating predominance of hillslope creep processes and higher values indicating vigorous erosion and gullying.

4.4. Climate Changes Decrease Landscape Stability

Relationships between global climate, local paleoenvironment, and erosion rate are demonstrated by comparing Sm/Kao and Ti in STL lake sediments to the paleoecology of STL (Jiménez-Moreno et al., 2023) and global climate indicators (Andersen et al., 2004; Barker et al., 2011; Lisiecki & Raymo, 2005; Figure 6). The highest erosion rates (high Ti) and gullying (high Sm/Kao) occur during the Last Interglacial (MIS 5), at the beginning and end of MIS 3 (a period of generally milder glacial conditions (Anderson et al., 2000; Jiménez-Moreno et al., 2023)), and during the Holocene (Figure 6). Erosion correlates with local occupations by either a piñon pine (*P. edulis*), juniper (*Juniperus*), and oak (*Quercus*) woodland or a ponderosa pine forest, drier conditions indicated by negative

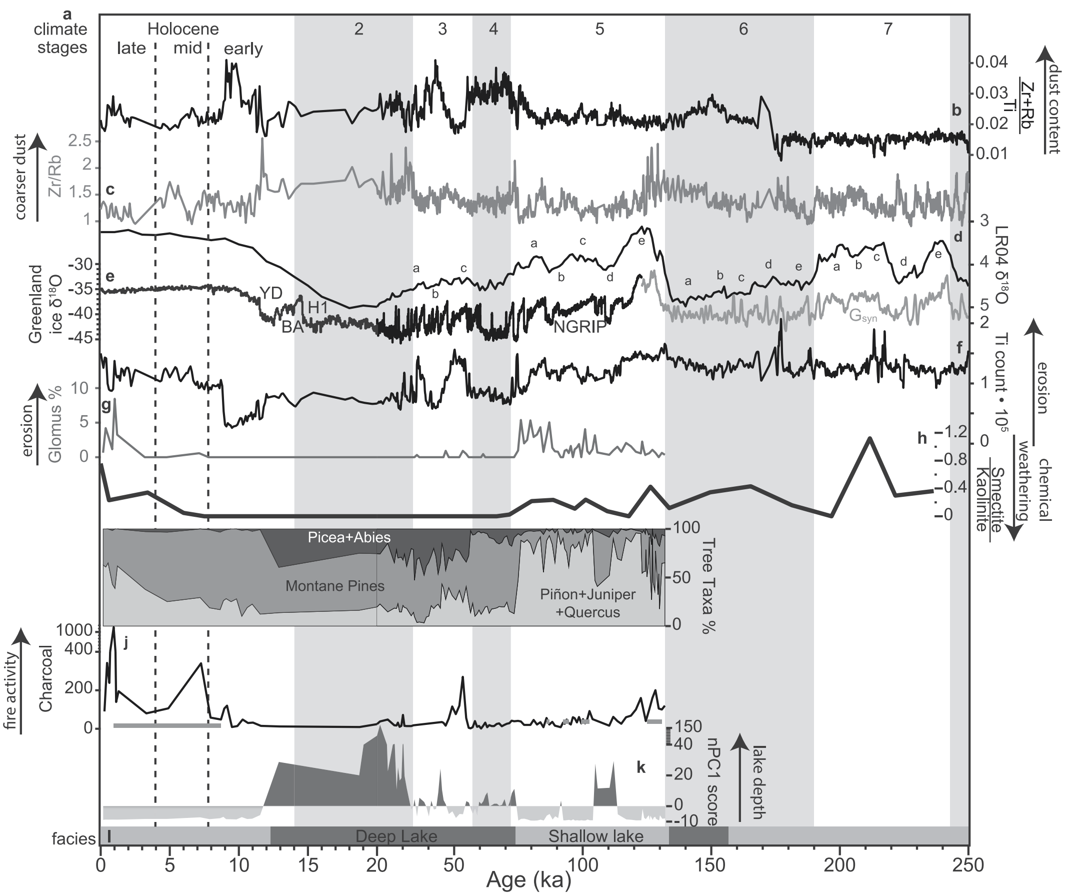

Figure 6. Erosion, ecology, and climatology at Stoneman Lake (STL). Note *x*-axis scale change at 20 ka. (a) Climate stages defined by Railsback et al. (2015) and correspond to shading. (b) (Zr + Rb)/Ti indicates clastic eolian content relative to local inputs while (c) Zr/Rb indicates eolian grain size. See text for details. (d) The LR04 marine benthic stack indicates global climate (Lisiecki & Raymo, 2005). Glacial-interglacial cycles are segmented into Marine Isotope Stages (a) subdivided into lettered substages. (e) NGRIP (Andersen et al., 2004) and Gsyn (Barker et al., 2011) track North Atlantic climate change. (f) Titanium (Ti) indicates erosion in the STL catchment. (g) Percent abundance of *Glomus*, an endomycorrhizal fungus indicates soil erosion and mechanical disturbance. (h) Smectite/kaolinite may indicate depth of erosion. (i) Relative percent abundance of tree taxa including thermophiles: *P. edulis*, *Juniperus*, and *Quercus*, more mesic montane pine taxa: *P. indeterminant* (ponderosa, limber, SW white, and/or lodgepole), and boreal taxa: *Picea* and *Abies*. (j) Charcoal particle count, an indicator of forest fire activity. Gray bars denote large (60–100 μm) particle size, an indicator of intense local fires. (k) non-pollen palynomorph principal component analysis score (nPC1). nPC1+ combines *Pediastrum*, *Isoetes*, *Filinia longiseta*, and *Botryococcus*, indicators of deep oligotrophic waters. nPC1- combines *Zygnema*, *Spirogyra*, *Debarya*, *Neorhabdocoela*, and *Glomus*, indicators of shallow meso- to eutrophic water. Panels (g, i–k) data are from Jiménez-Moreno et al. (2023). (l) Simplified facies of Staley et al. (2022) indicating lake depth.

nPC1 (nPC1−) scores, and high wildfire activity indicated by charcoal counts (Figure 6). Increased precipitation intensity in the form of summer convective storms (Betancourt et al., 1990; Cisneros-Dozal et al., 2014; Insel & Berkelhammer, 2021) and tropical cyclones (Barron et al., 2012; Roy et al., 2017) likely also contributes to erosion via increases in surface runoff. Conversely, glacial periods MIS 2 and 4 exhibit much lower Ti and Sm/Kao correlating hillslope stability and dominance of hillslope creep to cooler and wetter conditions, the expansion of subalpine forests containing spruce (*Picea*) and fir (*Abies*) around STL, deeper, oligotrophic lake water (nPC1+), and reduced wildfire activity (Figure 6). Glacial precipitation in SWNA is characterized by protracted but low intensity winter rain and snow events that favor infiltration over runoff (Jiménez-Moreno et al., 2023; Kohn et al., 2022; Oster et al., 2015; Palecki et al., 2005; Wendt et al., 2018). Thus, vegetation, precipitation mode, and forest fire regime appear to work in tandem to influence erosion rates and landscape stability at STL.

We have thus linked erosional patterns in the STL catchment to the two broadly defined Quaternary climate endmembers: warmer-drier interglacials and cooler-wetter glacial periods. However, further insights can be gleaned from the STL14 record regarding how abrupt (sub-millennial timescale) climate changes in the past have affected strong sedimentary responses, and therefore how this landscape might respond to rapid modern aridification and increases in forest fire activity. The MIS 6 > 5 transition at 132 ka is one such abrupt event. While palynological analysis of MIS 6, the penultimate glacial period, is forthcoming, it indicates that fir, spruce, and montane pines grew near STL. Following the MIS 6 > 5 transition, forest displacement by piñon and juniper and an increase in fire activity correlates to peak Ti and Sm/Kao at ~130 ka (Figure 6). Jiménez-Moreno et al. (2023) invoke intense erosion during MIS 5e and remobilization of pollen previously trapped in soils as an explanation for the presence of subalpine tree pollen well into the interglacial despite all other evidence pointing to peak warmth and aridity. Considering that local sediment production likely increases during glacials due to increased moisture and frost action, reduced sediment transport during these same periods likely results in the formation of thick clay-rich hillslope soils. Therefore, much of the local smectite-rich sediment deposited into the lake during the early parts of subsequent interglacials was likely produced during the previous glacial period.

Following the dramatic changes of early MIS 5, STL experienced further variability related to precession-driven climate oscillations. The transition from MIS 5d > c at 106 ka is particularly informative to future predictions and may be analogous to changes occurring today on the Colorado Plateau, where montane pine forests developed during the Late Holocene (Figure 6) are now being threatened by forest fires and displacement by the piñon-juniper woodland. Before this transition, cooler and wetter conditions of MIS 5d were marked by an expansion of the montane pine forest, a deeper lake (facies and nPC1+), and lower erosion rates signaled by decreased Ti, Sm/Kao, and *Glomus* (Figure 6). At the transition into MIS 5c, increased warmth and aridity resulted in increased erosion rates despite lower amplitude climate changes compared with glacial Termination II.

The MIS 5 > 4 transition (72 ka) into glacial conditions is indicated by a deepening lake (bedded facies, nPC1+) and replacement of piñon-juniper woodland by montane pine and some subalpine pollen (Figure 6). We observe decreased erosion rates for the remainder of MIS 4, likely stemming from greater vegetative cover and decreased fire activity; however, Ti shows a short-lived peak at the MIS 5 > 4 boundary suggesting an increase in effective precipitation caused a brief period of geomorphic adjustment and enhanced erosion (Figure 6f). This is intriguing because it suggests that abrupt climate change, regardless of the direction, promotes enhanced erosion rates. McAuliffe et al. (2006) showed that on decadal to centennial timescales, vegetation loss caused by drought can exacerbate erosion rates when precipitation eventually increases. Here, the short-lived increase in Ti shows that higher effective precipitation is associated only with increased erosion rates in this hillslope dominated catchment for at most a few thousand years (Figure 6f), perhaps related to a brief successional period where colonization by new vegetation communities lagged climatic changes.

The next major change occurs at the MIS 4 > 3 transition (57 ka) where an abrupt reversal away from glacial conditions is indicated by lake shallowing (facies, nPC1−), a decrease in montane pine pollen, and an increase in fire activity to peak values (Figure 6). These changes appear to have led to enhanced erosion; Ti is higher than at any point during the Last Glacial (MIS 4–2). Thousands of years later, near the end of MIS 3, a similar, shorter-lived increase in erosion occurs during the MIS 3b > a transition (38 ka). Here, higher erosion rates correlate with increased effective precipitation, montane pine and subalpine pollen, and reduced fire activity, an opposite climatic change from the previous transition. This provides additional evidence that abrupt climatic and ecological transitions of any kind can result in decreased landscape stability and higher erosion rates.

One of the best studied climate transitions in SWNA is the Pleistocene-Holocene transition (PHT) beginning at 14 ka. The PHT is associated with dramatic erosion of hillslope soils in what are now deserts of SWNA (Antinao & McDonald, 2013; Bull, 1991; D'Arcy et al., 2017; Miller et al., 2010). Ti values in STL core sediments remain low following the PHT despite a rapid warming and drying transition suggested by nPC1- and decreased subalpine pollen (Figure 6). While this suggests that erosion rates remained low from 14 to 8 kyr, higher levels of TOC (5%–20%) during this interval (Figure 5) could be masking the erosion signal by dilution. While a brief increase in Ti occurs during the Younger Dryas (12.9–11.7 ka) (Figure 6f), this could be a result of decreased productivity, indicated by a slight decrease in TOC, during this millennial scale cold event rather than increased erosion (Figure 5). The absence of *Glomus* and low Sm/Kao ratios support interpretations of modest erosion rates (Figures 6g and 6h). The middle Holocene is driest both at STL and regionally (Anderson, 1993; Antevs, 1948; Hasbargen, 1994; Lachniet et al., 2020; Staley et al., 2022). At its outset (ca. 8 ka), a significant increase in erosion (Ti, Sm/Kao, and *Glomus*) is associated with a large increase in nearby fire activity, as shown by charcoal counts (Figure 6). This suggests that enhanced erosion rates in the STL catchment during the Holocene may have been contingent on fire activity, which had been lower in the Early Holocene. Significant peaks in Ti, *Glomus*, and charcoal occur within the last 1.5 kyr (Figure 6) and could relate to activities of Indigenous peoples on the Mogollon Rim (Roos et al., 2022).

4.5. Eolian Signals

Quartz and illite are not physical or chemical weathering products of basalt, yet they comprise a significant portion of the fine material in catchment colluvium and a majority of lake sediments through time (Figure 2). These minerals, in addition to trace quantities of zircon, must be eolian. Ternary plots (Figures 4d and 4e) show the geochemical compositions of catchment colluvium between local bedrock and regional dusts. In both plots, dust and upper continental crust occupy similar geochemical space reflecting their felsic composition and genetic linkage (Taylor et al., 1983). In Al-K-Ti space, Al behaves conservatively as samples trend from high-Ti, low-K basalt to low-Ti, hi-K dust (Figure 4d). Illite, a slightly altered muscovite ($KAl_2(AlSi_3O_{10})(OH)_2$), is likely responsible for K enrichment in colluvium, although upward transfer of this important nutrient by root uptake could also be a contributing factor (Jobbágy & Jackson, 2001).

We use geochemical relationships to show that (Zr + Rb)/Ti in XRF core scans is an indicator of dust deposition relative to local clastics and Zr/Rb indicates dust grain size (e.g., Calvert & Pedersen, 2007; Chen et al., 2006). Zr-Rb-Ti ternary space shows that colluvium contains dust, enriched in eolian Zr and Rb compared to Ti-rich local bedrock (Figure 4e). Zr enrichment in colluvium and regional dusts is due to the presence of zircon ($ZrSiO_4$) which dominates bulk Zr concentrations whenever present (Balan et al., 2001; Milnes & Fitzpatrick, 1989; Tole, 1985). Zircons form very fine sand-to-silt sized crystals in granitic rocks (Taboada et al., 2006) and are resistant to chemical and biological processes at Earth's surface, concentrating into sedimentary residuals. Despite their high density relative to other common eolian minerals, fine zircons can remain suspended in the atmosphere thousands of kilometers from their source (Aarons et al., 2013). Upwind zircon source rocks are widespread in Nevada, California, and Arizona in the deserts of the Basin and Range province. The influence of zircons on the elemental composition of colluvium indicates that using Zr as a normalizing immobile element when dust inputs are significant confounds calculations of chemical and physical erosion rates using chemical depletion fraction techniques (e.g., Riebe et al., 2004). The large spread in Zr concentrations of regional dusts (Figure 4e) may reflect variable concentrations in dust sources and/or density fractionation of zircons during transport. Therefore, Zr concentrations in STL colluvium and lake sediments are associated with coarser-grained dust content. Rb is also linked to dust, and like K, is probably associated with illite. Rb is an incompatible element that partitions into igneous melts, causing it to concentrate in felsic rocks rather than mantle basalts. Rb substitutes for K in aluminosilicates, particularly in micaceous minerals (Calvert & Pedersen, 2007). Unlike Zr, Rb does not fractionate into heavy minerals, explaining its confined range of concentrations in regional dusts (Figure 4e); therefore, it can be used to trace finer grained eolian material. In a subsequent paper we will test these geochemical indicators using direct grain size measurements.

Relative—and it should be emphasized, not absolute—dust inputs measured by (Zr + Rb)/Ti are higher during glacials (MIS 6, 4, and 2) than interglacials (MIS 7, 5, and 1) (Figure 6b). Despite the potential for enhanced dust fertilization during glacials, STL remained oligotrophic (nPC1+). Sediments from MIS 3 exhibit a high range of dust fractions through time. Toward the end of glacial periods MIS 2 and 6, the dust fraction declines slightly from peak glacial values. Following the PHT, the dust fraction returns to peak values, perhaps signaling increased dust production upwind. Our record of dust content for the Holocene is similar to dust accumulation rates in Montezuma Well, a sinkhole depression 25 km to the SW of STL (Tau et al., 2021). Both records show increases during the Early Holocene, a Middle Holocene lull, and a modest increase during the Late Holocene (Figure 6b). A similar peak is not present after the penultimate glacial termination (MIS 6 > 5) at ~132 ka.

Larger dust grain sizes (higher Zr/Rb) appear to define the later stages of MIS 6, the start of MIS 5e, MIS 2, and immediately after the PHT (Figure 6c). Influxes of coarser dust during these times could signal two separate phenomena: intensified westerly atmospheric circulation during glacials (Abell et al., 2021; Li et al., 2022; Oster et al., 2015) and/or activation of nearby dust sources in the floodplains and piedmonts of the middle Verde River Valley. Rivers across the Colorado Plateau aggrade during glacial periods, exposing fine sediments on their floodplains to the atmosphere (Anders et al., 2005; Ellwein et al., 2011; Malmon et al., 2011). At the moment, we cannot determine the causes of this variability, nor can we quantify dust accumulation rates. In subsequent research, we will perform grain size analysis and determine dust mass accumulation rates in the STL14 core record, potentially revealing dust emission patterns relating to erosion and exposure of fine sediments in the vast desert regions and rivers upwind to the west and south.

5. Conclusion

Geochemical analyses of bedrock and colluvium from the STL catchment indicate that chemical dissolution of minerals such as olivine, pyroxene, and Ca-plagioclase likely drives sediment production by exposing more resistant minerals such as Na-plagioclase and ilmenite to physical removal. Chemical weathering produces secondary clay minerals such as montmorillonite as well as other amorphous weathering products. Increased local geomorphic stability during wetter glacial periods results from increased vegetative cover provided by montane and subalpine forests, fewer intense forest fires, and less intense precipitation modes. Erosional processes were enhanced during warmer and drier interglacial conditions in response to decreased vegetative cover, increased forest fire activity, and more intense precipitation events. Significant and persistent dust inputs to STL occur over the last few glacial cycles, suggesting that dust is constantly deposited across the broader Colorado Plateau region. Relative to local sedimentary inputs, dust input varies at glacial to millennial timescales.

Core STL14 archives multiple interconnected critical zone processes operating at STL over glacial-interglacial timescales and shows this landscape is sensitive to climate change. While increased effective precipitation can temporarily increase erosion, shifts toward warmer and drier conditions, and especially increases in forest fire activity, are responsible for lasting increases in erosion rates. The highest levels of wildfire activity and erosion occur during periods of greatest warmth, aridity, and vegetation turnover. Glacial terminations such as the PHT may not be the best analogs for the impact of ongoing climate change on erosion because the modern landscape does not have the large stores of sediment in thick soils that develop during glacials. In our record, the MIS 5d > c transition is perhaps the most analogous to modern conditions and shows that interglacial climate oscillations, mild in comparison to glacial-interglacial shifts, can enhance erosion rates. Given these results and an expectation of continued anthropogenic warming and aridification, we expect erosion rates within the STL catchment to remain high and perhaps increase in the future. Although these findings are from a relatively steep basaltic terrain currently situated in a semi-arid montane forest of ponderosa pine, similar settings are widespread across the Colorado Plateau. Areas experiencing increased forest fire activity and changeover from subalpine/montane to piñon-juniper forest communities are likely to experience increased erosion in the centuries and millennia to come.

Acknowledgments

The authors are greatly appreciative of the insightful and thorough comments made by Martha-Cary Eppes and two other anonymous peer-reviewers. Their reviews significantly improved the substance and clarity of the manuscript. SES and PJF wish to acknowledge the staff and facilities at the CSD Facility (formerly LACCORE) at the University of Minnesota, Dr. Robert Brown at the XRF Laboratory of the Large Lakes Observatory at the University of Minnesota, Duluth, Dr. Abdul-Mehdi Ali of UNM's Analytical Chemistry Laboratory, Mike Spilde of UNM's Electron Microbeam Facility, and Dr. Eric Peterson of UNM's X-Ray Diffraction Laboratory/Center for Micro-Engineered Materials for their assistance with data collection. RSA wishes to acknowledge assistance from the US Forest Service for core collection, and Pilot Grant Program (PGP) grant from NAU for coring funding. GJM acknowledges funding from the Ministerio de Ciencia, Innovación y Universidades, Grants PRX18/00080 and PRX21/00127, for "Salvador de Madariaga" research stays at UNM and NAU for the sampling and treatment of sediment core samples for pollen extraction and pollen analysis. RSA acknowledges a grant from the Arizona TRIF research program (Project 1002654); "Mega-droughts, climate change and the Southwest: STL, AZ, Paleoenvironments Drilling Project".

Data Availability Statement

Stratigraphic data from core STL14 including radiocarbon ages, Bayesian age model output, color, sedimentary facies, composition (TOC, density, Magnetic susceptibility, XRF geochemistry are available at https://doi.org/10.25921/kq32-d134, Staley et al., 2023), within NOAA's NCEI Paleo Data repository (https://www.ncei.noaa.gov/products/paleoclimatology). Geochemical and mineralogical data of Stoneman Lake catchment bedrock and colluvium is available at https://doi.org/10.26022/IEDA/113008 (Staley, 2023), within Lamont-Doherty Earth Observatory's EarthChem database (https://earthchem.org/).

Bayesian age model was generated using Bacon (Blaauw & Christen, 2012) version 2.3.9.1, a program run on R software (https://cran.r-project.org/bin/windows/base/), both freely accessible. Figures were made using MATLAB R2022a (https://www.mathworks.com/products/matlab.html) and Adobe Illustrator 2023 (https://www.adobe.com/products/illustrator.html), both requiring a license to download and use.

References

Aarons, S. M., Aciego, S. M., & Gleason, J. D. (2013). Variable Hf-Sr-Nd radiogenic isotopic compositions in a Saharan dust storm over the Atlantic: Implications for dust flux to oceans, ice sheets and the terrestrial biosphere. *Chemical Geology*, *349–350*, 18–26. https://doi.org/10.1016/j.chemgeo.2013.04.010

Aarons, S. M., Blakowski, M. A., Aciego, S. M., Stevenson, E. I., Sims, K. W. W., Scott, S. R., & Aarons, C. (2017). Geochemical characterization of critical dust source regions in the American West. *Geochimica et Cosmochimica Acta*, *215*, 141–161. https://doi.org/10.1016/j.gca.2017.07.024

Abell, J. T., Winckler, G., Anderson, R. F., & Herbert, T. D. (2021). Poleward and weakened westerlies during Pliocene warmth. *Nature*, *589*(7840), 70–75. https://doi.org/10.1038/s41586-020-03062-1

Anders, M. D., Pederson, J. L., Rittenour, T. M., Sharp, W. D., Gosse, J. C., Karlstrom, K. E., et al. (2005). Pleistocene geomorphology and geochronology of eastern Grand Canyon: Linkages of landscape components during climate changes. *Quaternary Science Reviews*, *24*(23–24), 2428–2448. https://doi.org/10.1016/j.quascirev.2005.03.015

Andersen, K. K., Azuma, N., Barnola, J. M., Bigler, M., Biscaye, P., Caillon, N., et al. (2004). High-resolution record of Northern Hemisphere climate extending into the last interglacial period. *Nature*, *431*(7005), 147–151. https://doi.org/10.1038/nature02805

Anderson, R. S. (1993). A 35,000 year vegetation and climate history from Potato Lake, Mogollon Rim, Arizona. *Quaternary Research*, *40*(3), 351–359. https://doi.org/10.1006/qres.1993.1088

Anderson, R. S., Betancourt, J. L., Mead, J. I., Hevly, R. H., & Adam, D. P. (2000). Middle- and Late-Wisconsin paleobotanic and paleoclimatic records from the southern Colorado Plateau, USA. *Palaeogeography, Palaeoclimatology, Palaeoecology*, *155*(1–2), 31–57. https://doi.org/10.1016/s0031-0182(99)00093-0

Antevs, E. (1948). The Great Basin, with emphasis on glacial and post-glacial times; Climatic changes and pre-white man. *Bulletin of the University of Utah*, *38*, 168–191.

Antinao, J. L., & McDonald, E. (2013). A reduced relevance of vegetation change for alluvial aggradation in arid zones. *Geology*, *41*(1), 11–14. https://doi.org/10.1130/g33623.1

Ashley, G. M. (2020). Paleo-Critical Zones, windows into the changing life and landscapes during the Quaternary Period. *Quaternary Research*, *96*, 53–65. https://doi.org/10.1017/qua.2020.49

Balan, E., Trocellier, P., Jupille, J., Fritsch, E., Muller, J.-P., & Calas, G. (2001). Surface chemistry of weathered zircons. *Chemical Geology*, *181*(1–4), 13–22. https://doi.org/10.1016/s0009-2541(01)00271-6

Barker, S., Knorr, G., Edwards, R. L., Parrenin, F., Putnam, A. E., Skinner, L. C., et al. (2011). 800,000 years of abrupt climate variability. *Science*, *334*(6054), 347–351. https://doi.org/10.1126/science.1203580

Barron, J. A., Metcalfe, S. E., & Addison, J. A. (2012). Response of the North American monsoon to regional changes in ocean surface temperature. *Paleoceanography*, *27*, PA3206. https://doi.org/10.1029/2011pa002235

Betancourt, J. L., Van Devender, T. R., & Martin, P. S. (1990). *Packrat middens: The last 40,000 years of biotic change*. University of Arizona Press.

Birkeland, P. W. (1999). *Soils and geomorphology* (3rd ed.). Oxford University Press.

Blaauw, M., & Christen, J. A. (2012). Bacon manual. 2.3.9.1 (pp. 1–15).

Blasch, K. W., Hoffmann, J. P., Graser, L. F., Bryson, J. R., & Flint, A. L. (2006). Hydrogeology of the upper and middle Verde River watersheds, central Arizona. In *U.S.G.S. scientific investigations report 2005–5198* (p. 102).

Blum, A. E., & Stillings, L. L. (1995). Feldspar dissolution kinetics. In A. F. White & S. L. Brantley (Eds.), *Chemical weathering rates of silicate minerals* (pp. 118–172). Mineralogical Society of America.

Bradford, J. B., Betancourt, J. L., Butterfield, B. J., Munson, S. M., & Wood, T. E. (2018). Anticipatory natural resource science and management for a changing future. *Frontiers in Ecology and the Environment*, *16*(5), 295–303. https://doi.org/10.1002/fee.1806

Bradford, J. B., Schlaepfer, D. R., Lauenroth, W. K., & Palmquist, K. A. (2020). Robust ecological drought projections for drylands in the 21st century. *Global Change Biology*, *26*(7), 3906–3919. https://doi.org/10.1111/gcb.15075

Brimhall, G. H., & Dietrich, W. E. (1987). Constitutive mass balance relations between chemical composition, volume, density, porosity, and strain in metasomatic hydrochemical systems: Results on weathering and pedogenesis. *Geochimica et Cosmochimica Acta*, *51*(3), 567–587. https://doi.org/10.1016/0016-7037(87)90070-6

Brown, D. E. (1982). Biotic communities of the American southwest-United States and Mexico. *Desert plants*, *4*(1–4), 343.

Bull, W. B. (1991). *Geomorphic responses to climate change*. Oxford University Press.

Burns, R. M., & Honkala, B. H. (1990). *Silvics of North America, Volume 1, Conifers*. USDA Forest Service.

Calvert, S. E., & Pedersen, T. F. (2007). Elemental Proxies for Palaeoclimatic and Palaeoceanographic variability in marine sediments: Interpretation and application. In *Developments in marine geology* (Vol. 1, pp. 567–644).

Chen, J., Chen, Y., Liu, L., Ji, J., Balsam, W., Sun, Y., & Lu, H. (2006). Zr/Rb ratio in the Chinese loess sequences and its implication for changes in the East Asian winter monsoon strength. *Geochimica et Cosmochimica Acta*, *70*(6), 1471–1482. https://doi.org/10.1016/j.gca.2005.11.029

Cisneros-Dozal, L. M., Huang, Y., Heikoop, J. M., Fawcett, P. J., Fessenden, J., Anderson, R. S., et al. (2014). Assessing the strength of the monsoon during the Late Pleistocene in southwestern United States. *Quaternary Science Reviews*, *103*, 81–90. https://doi.org/10.1016/j.quascirev.2014.08.022

Claquin, T., Schulz, M., & Balkanski, Y. J. (1999). Modeling the mineralogy of atmospheric dust sources. *Journal of Geophysical Research*, *104*(D18), 22243–22256.

Colman, S. M. (1982). Chemical weathering of basalts and andesites: Evidence from weathering rinds. In *Geological survey professional paper 1246* (p. 51).

D'Arcy, M., Roda-Boluda, D. C., & Whittaker, A. C. (2017). Glacial-interglacial climate changes recorded by debris flow fan deposits, Owens Valley, California. *Quaternary Science Reviews*, *169*, 288–311. https://doi.org/10.1016/j.quascirev.2017.06.002

Davenport, D. W., Breshears, D. D., Wilcox, B. P., & Allen, C. D. (1998). Viewpoint: Sustainability of piñon-juniper ecosystems-a unifying perspective of soil erosion thresholds. *Journal of Range Management*, *51*(2), 231–240. https://doi.org/10.2307/4003212

Davison, W. (1993). Iron and manganese in lakes. *Earth-Science Reviews*, *34*(2), 119–163. https://doi.org/10.1016/0012-8252(93)90029-7

Dohm, J. M. (1995). *Origin of Stoneman Lake, and volcano-tectonic relations of Mormon and San Francisco volcanic fields, Arizona* (M.S. thesis). Northern Arizona University.

East, A. E., & Sankey, J. B. (2020). Geomorphic and sedimentary effects of modern climate change: Current and anticipated future conditions in the western United States. *Reviews of Geophysics*, *58*(4), e2019RG000692. https://doi.org/10.1029/2019rg000692

Eggleton, R. A., Foudoulis, C., & Varkevisser, D. (1987). Weathering of basalt: Changes in rock chemistry and mineralogy. *Clays and Clay Minerals*, *35*(3), 161–169. https://doi.org/10.1346/ccmn.1987.0350301

Ellwein, A. L., Mahan, S. A., & McFadden, L. D. (2011). New optically stimulated luminescence ages provide evidence of MIS3 and MIS2 eolian activity on Black Mesa, northeastern Arizona, USA. *Quaternary Research*, *75*(3), 395–398. https://doi.org/10.1016/j.yqres.2010.12.002

Eppes, M. C., & Keanini, R. (2017). Mechanical weathering and rock erosion by climate-dependent subcritical cracking. *Reviews of Geophysics*, *55*(2), 470–508. https://doi.org/10.1002/2017rg000557

Goldich, S. S. (1938). A study in rock-weathering. *The Journal of Geology*, *46*(1), 17–58. https://doi.org/10.1086/624619

Gust, D. A., & Arculus, R. J. (1986). Petrogenesis of alkalic and calcalkalic volcanic rocks of Mormon Mountain Volcanic Field, Arizona. *Contributions to Mineralogy and Petrology*, *94*(4), 416–426. https://doi.org/10.1007/bf00376335

Gyssels, G., Poesen, J., Bochet, E., & Li, Y. (2005). Impact of plant roots on the resistance of soils to erosion by water: A review. *Progress in Physical Geography*, *29*(2), 189–217. https://doi.org/10.1191/0309133305pp443ra

Hanks, J. P., Fitzhugh, E. L., & Hanks, S. R. (1983). A habitat type classification system for ponderosa pine forests of Northern Arizona. In *USDA forest service, general technical report RM-97* (pp. 1–22).

Hasbargen, J. (1994). A Holocene paleoclimatic and environmental record from Stoneman Lake, Arizona. *Quaternary Research*, *42*(2), 188–196. https://doi.org/10.1006/qres.1994.1068

Haug, G. H., Gunther, D., Peterson, L. C., Sigman, D. M., Hughen, K. A., & Aeschlimann, B. (2003). Climate and the collapse of Maya civilization. *Science*, *299*(5613), 1731–1735. https://doi.org/10.1126/science.1080444

Heckman, K., & Rasmussen, C. (2011). Lithologic controls on regolith weathering and mass flux in forested ecosystems of the southwestern USA. *Geoderma*, *164*(3–4), 99–111. https://doi.org/10.1016/j.geoderma.2011.05.003

Hereford, R. (2007). Climate variation at Flagstaff, Arizona—1950 to 2007. In *USGS open-file report 2007–1410* (pp. 1–17).

Hereford, R., & Amoroso, L. (2020). Historical and prehistorical water levels of Mormon Lake, Arizona as a measure of climate change on the southwest Colorado Plateau, USA. *Quaternary Research*, *100*, 32–51. https://doi.org/10.1017/qua.2020.92

Holm, R. F., Nealey, L. D., Conway, F. M., & Ulrich, G. E. (1989). Mormon Lake volcanic field. In C. E. Chapin & J. Zidek (Eds.), *Field excursions to volcanic terranes in the western United States, v. 1: Southern Rocky mountain region: New Mexico Bureau of mines and mineral resources, memoir 46* (pp. 2–9).

Insel, N., & Berkelhammer, M. (2021). The influence of orbital parameters on the North American monsoon system during the Last interglacial period. *Journal of Quaternary Science*, *36*(4), 638–648. https://doi.org/10.1002/jqs.3311

Jiménez-Moreno, G., Anderson, R. S., Markgraf, V., Staley, S. E., & Fawcett, P. J. (2023). Environmental and climate evolution in the Southwest USA since the Last interglacial deduced from the pollen record from Stoneman Lake, Arizona. *Quaternary Science Reviews*, *300*(107883), 1–15. https://doi.org/10.1016/j.quascirev.2022.107883

Jobbágy, E. G., & Jackson, R. B. (2001). The distribution of soil nutrients with depth: Global patterns and the imprint of plants. *Biogeochemistry*, *53*(1), 51–77. https://doi.org/10.1023/a:1010760720215

Kohn, M. J., Springer, K. B., Pigati, J. S., Reynard, L. M., Drewicz, A. E., Crevier, J., & Scott, E. (2022). Seasonality of precipitation in the southwestern United States during the late Pleistocene inferred from stable isotopes in herbivore tooth enamel. *Quaternary Science Reviews*, *296*, 1–21. https://doi.org/10.1016/j.quascirev.2022.107784

Lachniet, M. S., Asmerom, Y., Polyak, V., & Denniston, R. (2020). Great Basin paleoclimate and aridity linked to arctic warming and tropical Pacific sea surface temperatures. *Paleoceanography and Paleoclimatology*, *35*(7), e2019PA003785. https://doi.org/10.1029/2019pa003785

Lawrence, C. R., Painter, T. H., Landry, C. C., & Neff, J. C. (2010). Contemporary geochemical composition and flux of aeolian dust to the San Juan Mountains, Colorado, United States. *Journal of Geophysical Research*, *115*(G3), G03007. https://doi.org/10.1029/2009jg001077

Li, Y., Peng, S., Hao, L., Zhou, X., & Li, H. (2022). Interactions of the westerlies and Asian summer monsoon since the last deglaciation in the northeastern Qinghai-Tibet Plateau. *Paleoceanography and Paleoclimatology*, *37*(11), e2022PA004548. https://doi.org/10.1029/2022pa004548

Lisiecki, L. E., & Raymo, M. E. (2005). A Pliocene-Pleistocene stack of 57 globally distributed benthic $\delta^{18}O$ records. *Paleoceanography*, *20*(1), PA1003. https://doi.org/10.1029/2004pa001071

MacDonald, L. H., & Huffman, E. L. (2004). Post-fire soil water repellency. *Soil Science Society of America Journal*, *68*(5), 1729–1734. https://doi.org/10.2136/sssaj2004.1729

Makri, S., Wienhues, G., Bigalke, M., Gilli, A., Rey, F., Tinner, W., et al. (2021). Variations of sedimentary Fe and Mn fractions under changing lake mixing regimes, oxygenation and land surface processes during Late-glacial and Holocene times. *Science of the Total Environment*, *755*, 1–12. https://doi.org/10.1016/j.scitotenv.2020.143418

Malmon, D. V., Howard, K. A., House, P. K., Lundstrom, S. C., Pearthree, P. A., Sarna-Wojcicki, A. M., et al. (2011). Stratigraphy and depositional environments of the upper Pleistocene Chemehuevi Formation along the Lower Colorado river. In *U.S.G.S. Professional paper 1786* (p. 95).

Marshall, J. A., Roering, J. J., Rempel, A. W., Shafer, S. L., & Bartlein, P. J. (2021). Extensive frost weathering across unglaciated North America during the Last Glacial Maximum. *Geophysical Research Letters*, *48*(5), 1–12. https://doi.org/10.1029/2020gl090305

McAuliffe, J. R., Scuderi, L. A., & McFadden, L. D. (2006). Tree-ring record of hillslope erosion and valley floor dynamics: Landscape responses to climate variation during the last 400 yr in the Colorado Plateau, northeastern Arizona. *Global and Planetary Change*, *50*(3–4), 184–201. https://doi.org/10.1016/j.gloplacha.2005.12.003

McCabe, K. W. (1971). *Geology and botany of Stoneman Lake Area, Coconino County* (M.S. Thesis). Northern Arizona University.

Miller, D. M., Schmidt, K. M., Mahan, S. A., McGeehin, J. P., Owen, L. A., Barron, J. A., et al. (2010). Holocene landscape response to seasonality of storms in the Mojave Desert. *Quaternary International*, *215*(1–2), 45–61. https://doi.org/10.1016/j.quaint.2009.10.001

Milnes, A. R., & Fitzpatrick, R. W. (1989). Titanium and zirconium minerals. In *Minerals in soil environments-SSSA book series, no. 1* (2nd ed., pp. 1131–1205). Soil Science Society of America.

Mitchell, J. E., & Roberts, T. C., Jr. (1999). Distribution of Pinyon-Juniper in the western United States. In S. B. Monsen & R. Stevens (Eds.), *Proceedings: Ecology and management of pinyon-juniper communities within the Interior West* (pp. 146–154). USDA Forest Service Proceedings RMRS-P-9.

Moore, D. M., & Reynolds, R. C. (1997). *X-ray diffraction and the identification and analysis of clay minerals* (2nd ed.). Oxford University Press.

Muhs, D. R., & Benedict, J. B. (2006). Eolian additions to Late Quaternary Alpine soils, Indian peaks wilderness area, Colorado front range. *Arctic Antarctic and Alpine Research*, *38*(1), 120–130. https://doi.org/10.1657/1523-0430(2006)038[0120:eatlqa]2.0.co;2

Naeher, S., Gilli, A., North, R. P., Hamann, Y., & Schubert, C. J. (2013). Tracing bottom water oxygenation with sedimentary Mn/Fe ratios in Lake Zurich, Switzerland. *Chemical Geology*, *352*, 125–133. https://doi.org/10.1016/j.chemgeo.2013.06.006

Nara, Y., Morimoto, K., Yoneda, T., Hiroyoshi, N., & Kaneko, K. (2011). Effects of humidity and temperature on subcritical crack growth in sandstone. *International Journal of Solids and Structures*, *48*(7–8), 1130–1140. https://doi.org/10.1016/j.ijsolstr.2010.12.019

Navarre-Sitchler, A., Steefel, C. I., Sak, P. B., & Brantley, S. L. (2011). A reactive-transport model for weathering rind formation on basalt. *Geochimica et Cosmochimica Acta*, *75*(23), 7644–7667. https://doi.org/10.1016/j.gca.2011.09.033

Navarre-Sitchler, A., Steefel, C. I., Yang, L., Tomutsa, L., & Brantley, S. L. (2009). Evolution of porosity and diffusivity associated with chemical weathering of a basalt clast. *Journal of Geophysical Research*, *114*(F2), F02016. https://doi.org/10.1029/2008jf001060

Oster, J. L., Ibarra, D. E., Winnick, M. J., & Maher, K. (2015). Steering of westerly storms over western North America at the Last Glacial Maximum. *Nature Geoscience*, *8*(3), 201–205. https://doi.org/10.1038/ngeo2365

Palecki, M. A., Angel, J. R., & Hollinger, S. E. (2005). Storm precipitation in the United States. Part I: Meteorological characteristics. *Journal of Applied Meteorology*, *44*(6), 933–946. https://doi.org/10.1175/jam2243.1

Pearson, G. A. (1950). *Management of ponderosa pine in the Southwest*. USDA Forest Service, Agriculture Monograph No. 6 (p. 218)

Péwé, T. L., Péwé, E. A., Péwé, R. H., Journaux, A., & Slatt, R. M. (1981). Desert dust: Characteristics and rates of deposition in central Arizona. In *Geological Society of America special paper* (Vol. 186, pp. 169–190).
Post, J. E., & Bish, D. L. (1989). Rietveld refinement of crystal structures using Powder X-ray diffraction data. In D. L. Bish & J. E. Post (Eds.), *Modern powder diffraction. Reviews in mineralogy* (Vol. 20, pp. 277–308). Mineralogical Society of America.
Pregitzer, K. S., Deforest, J. L., Burton, A. J., Allen, M. F., Ruess, R. W., & Hendrick, R. L. (2002). Fine root architecture of Nine North American trees. *Ecological Monographs*, *72*(2), 293–309. https://doi.org/10.1890/0012-9615(2002)072[0293:fraonn]2.0.co;2
PRISM Climate Group. (2022). 30-year normals. Retrieved from https://prism.oregonstate.edu/normals/
Railsback, L. B., Gibbard, P. L., Head, M. J., Voarintsoa, N. R. G., & Toucanne, S. (2015). An optimized scheme of lettered marine isotope substages for the last 1.0 million years, and the climatostratigraphic nature of isotope stages and substages. *Quaternary Science Reviews*, *111*, 94–106. https://doi.org/10.1016/j.quascirev.2015.01.012
Rasmussen, C., McGuire, L., Dhakal, P., & Pelletier, J. D. (2017). Coevolution of soil and topography across a semiarid cinder cone chronosequence. *Catena*, *156*, 338–352. https://doi.org/10.1016/j.catena.2017.04.025
Raven, M., & Self, P. (2017). Outcomes of 12 years of the Reynolds Cup quantitative mineral analysis round robin. *Clays and Clay Minerals*, *65*(2), 122–134. https://doi.org/10.1346/ccmn.2017.064054
Reheis, M. C., Budahn, J. R., Lamothe, P. J., & Reynolds, R. L. (2009). Compositions of modern dust and surface sediments in the Desert Southwest, United States. *Journal of Geophysical Research*, *114*, F01028. https://doi.org/10.1029/2008jf001009
Reheis, M. C., & Kihl, R. (1995). Dust deposition in southern Nevada and California, 1984–1989: Relations to climate, source area, and source lithology. *Journal of Geophysical Research*, *100*(D5), 8893–8918. https://doi.org/10.1029/94jd03245
Riebe, C. S., Kirchner, J. W., & Finkel, R. C. (2004). Erosional and climatic effects on long-term chemical weathering rates in granitic landscapes spanning diverse climate regimes. *Earth and Planetary Science Letters*, *224*(3–4), 547–562. https://doi.org/10.1016/j.epsl.2004.05.019
Rietveld, H. M. (1969). A profile refinement method for nuclear and magnetic structures. *Journal of Applied Crystallography*, *2*(65), 65–71. https://doi.org/10.1107/s0021889869006558
Roos, C. I., Laluk, N. C., Reitze, W., & Davis, O. K. (2022). Stratigraphic evidence for culturally variable Indigenous fire regimes in ponderosa pine forests of the Mogollon Rim area, east-central Arizona. *Quaternary Research*, *113*, 1–18. https://doi.org/10.1017/qua.2022.61
Roy, P. D., Chávez-Lara, C. M., Beramendi-Orosco, L. E., Sánchez-Zavala, J. L., Muthu-Sankar, G., Lozano-Santacruz, R., et al. (2017). Paleohydrology of the Santiaguillo Basin (Mexico) since late last glacial and climate variation in southern part of western subtropical North America. *Quaternary Research*, *84*(3), 335–347. https://doi.org/10.1016/j.yqres.2015.10.002
Rudzitis, S., Reid, M. R., & Blichert-Toft, J. (2016). On edge melting under the Colorado Plateau margin. *Geochemistry, Geophysics, Geosystems*, *17*(7), 2835–2854. https://doi.org/10.1002/2016gc006349
Staley, S. E. (2018). Sedimentology and stratigraphy of core STL14: An early Pleistocene-to-present paleoclimate archive from Stoneman Lake, Arizona (M.S. thesis). University of New Mexico.
Staley, S. E. (2023). Major and trace element analyses of basalts and colluvium of the Stoneman Lake catchment, AZ, USA, Version 1.0 [Dataset]. Interdisciplinary Earth Data Alliance (IEDA). https://doi.org/10.26022/IEDA/113008
Staley, S. E., Fawcett, P. J., Anderson, R. S., & Jiménez-Moreno, G. (2022). Early Pleistocene-to-present paleoclimate archive for the American southwest from Stoneman Lake, Arizona, USA. *Geological Society of America Bulletin*, *134*(3–4), 791–814. https://doi.org/10.1130/b36038.1
Staley, S. E., Fawcett, P. J., Jiménez-Moreno, G., Anderson, R. S., Markgraf, V., & Brown, E. T. (2023). NOAA/WDS Paleoclimatology—Stoneman Lake Arizona, USA, magnetic susceptibility and XRF count data over the past 1.3 Ma [Dataset]. NOAA National Centers for Environmental Information. https://doi.org/10.25921/kq32-d134
Sweeney, M. R., McDonald, E. V., & Markley, C. E. (2013). Alluvial sediment or playas: What is the dominant source of sand and silt in desert soil vesicular a horizons, southwest USA. *Journal of Geophysical Research: Earth Surface*, *118*(1), 257–275. https://doi.org/10.1002/jgrf.20030
Taboada, T., Cortizas, A. M., García, C., & García-Rodeja, E. (2006). Particle-size fractionation of titanium and zirconium during weathering and pedogenesis of granitic rocks in NW Spain. *Geoderma*, *131*(1–2), 218–236. https://doi.org/10.1016/j.geoderma.2005.03.025
Tau, G., Crouvi, O., Enzel, Y., Teutsch, N., Ginoux, P., & Rasmussen, C. (2021). Shutting down dust emission during the middle Holocene drought in the Sonoran Desert, Arizona, USA. *Geology*, *49*, 857–861. https://doi.org/10.1130/g48550.1
Taylor, S. R., McLennan, S. M., & McCulloch, M. T. (1983). Geochemistry of loess, continental crustal composition and crustal model ages. *Geochimica et Cosmochimica Acta*, *47*(11), 1897–1905. https://doi.org/10.1016/0016-7037(83)90206-5
Tole, M. P. (1985). The kinetics of dissolution of zircon ($ZrSi0_4$). *Geochimica et Cosmochimica Acta*, *49*(2), 453–458. https://doi.org/10.1016/0016-7037(85)90036-5
USDA Forest Service. (2022). Coconino National forest. Retrieved from https://www.fs.usda.gov/coconino
Viles, H. A. (1990). The agency of organic beings: A selective review of recent work in biogeomorphology. In J. B. Thornes (Ed.), *Vegetation and erosion: Processes and environments* (pp. 5–25). Wiley.
Vingiani, S., Righi, O., Petit, S., & Terribile, F. (2004). Mixed-layer kaolinite-smectite minerals in a red-black soil sequence from basalt in Sardinia (Italy). *Clays and Clay Minerals*, *52*(4), 473–483. https://doi.org/10.1346/ccmn.2004.0520408
Wendt, K. A., Dublyansky, Y. V., Moseley, G. E., Edwards, R. L., Cheng, H., & Spötl, C. (2018). Moisture availability in the southwest United States over the last three glacial-interglacial cycles. *Science Advances*, *4*(10), 1–8. https://doi.org/10.1126/sciadv.aau1375
Western Regional Climate Center. (2022). Climate summaries. Retrieved from https://wrcc.dri.edu/
Williams, J. A., & Anderson, T., Jr. (1967). Soil survey of Beaver Creek Area, Arizona. Retrieved from https://websoilsurvey.nrcs.usda.gov/

References From the Supporting Information

Brindley, G. B., & Brown, G. (1980). *Crystal structures of Clay minerals and their X-ray identification*. The Mineralogical Society.
Klug, H. P., & Alexander, L. E. (1974). *X-ray diffraction procedures: For polycrystalline and amorphous materials* (2nd ed.). Wiley.
Moseley, G. E., Edwards, R. L., Wendt, K. A., Cheng, H., Dublyansky, Y., Lu, Y., et al. (2016). Reconciliation of the Devils Hole climate record with orbital forcing. *Science*, *351*(6269), 165–168. https://doi.org/10.1126/science.aad4132
Reimer, P. J., Austin, W. E. N., Bard, E., Bayliss, A., Blackwell, P. G., Bronk Ramsey, C., et al. (2020). The IntCal20 Northern Hemisphere radiocarbon age calibration curve (0–55 cal kBP). *Radiocarbon*, *62*(4), 725–757. https://doi.org/10.1017/rdc.2020.41